Nano Research

ISSN 1998-0124 CN 11-5974/O4
https://doi.org/10.26599/NR.2025.94907784

A novel rock-salt structure high-entropy oxide $Fe_{0.2}Co_{0.2}Ni_{0.2}Cu_{0.2}Zn_{0.2}O$ as a highly reversible lithium storage material

Xiaobin He[1], Xuemei Zeng[1], Wei Wang[1], Yaqing Guo[1], Shengjie Zheng[1], Yun Li[1], Guixing Mo[1], Jiatong Zhang[1], Shun Wang[1], Hao Wang[2](✉), Yifei Yuan[1](✉)
[1] College of Chemistry and Materials Engineering, Wenzhou University, Wenzhou 325035, China
[2] Centre for Future Materials, University of Southern Queensland, Springfield, QLD 4300, Australia

Nano Res., **Just Accepted Manuscript** • https://doi.org/10.26599/NR.2025.94907784
https://www.sciopen.com/journal/1998-0124 on Jul. 9, 2025

© The Authors(s)

Just Accepted

This is a "Just Accepted" manuscript, which has been examined by the peer-review process and has been accepted for publication. A "Just Accepted" manuscript is published online shortly after its acceptance,which is prior to technical editing and formatting and author proofing. Tsinghua University Press (TUP) provides "Just Accepted" as an optional and free service which allows authors to make their results available to the research community as soon as possible after acceptance. After a manuscript has been technically edited and formatted, and the page proofs have been corrected, it will be removed from the "Just Accepted" web site and published officially with volume and article number (e.g., *Nano Research*, **2025**, *18*, 94906990). Please note that technical editing may introduce minor changes to the manuscript text and/or graphics which may affect the content, and all legal disclaimers that apply to the journal pertain. In no event shall TUP be held responsible for errors or consequences arising from the use of any information contained in these "Just Accepted" manuscripts. To cite this anuscript please use its Digital Object Identifier (DOI®),which is identical for all formats of publication.

Just Accepted

A novel rock-salt structure high-entropy oxide $Fe_{0.2}Co_{0.2}Ni_{0.2}Cu_{0.2}Zn_{0.2}O$ as a highly reversible lithium storage material

Xiaobin He[1], Xuemei Zeng[1], Wei Wang[1], Yaqing Guo[1], Shengjie Zheng[1], Yun Li[1], Guixing Mo[1], Jiatong Zhang[1], Shun Wang[1], Hao Wang[2]*, Yifei Yuan[1]*

[1] College of Chemistry and Materials Engineering, Wenzhou University, Wenzhou, Zhejiang 325035, China.

[2] Centre for Future Materials, University of Southern Queensland, Springfield, QLD 4300, Australia.

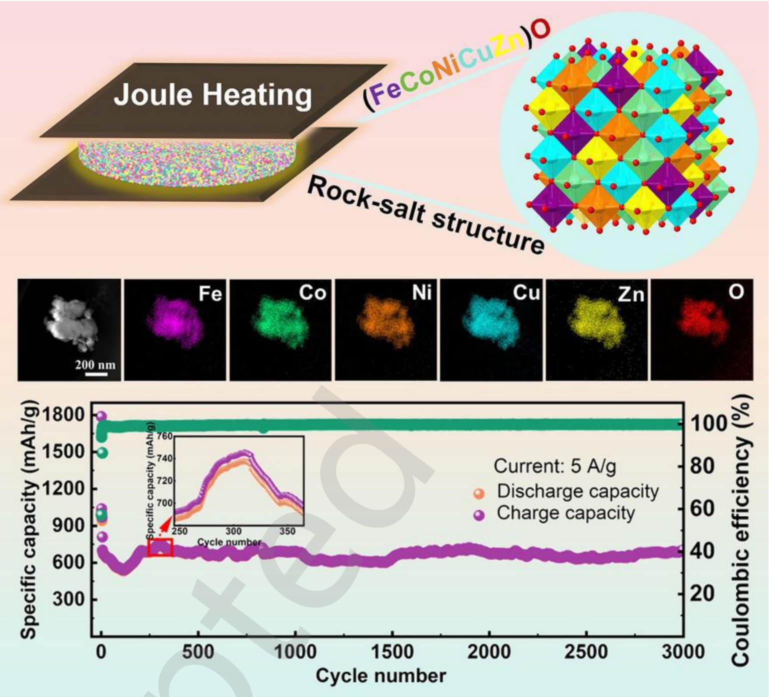

The rock-salt structure HEO $Fe_{0.2}Co_{0.2}Ni_{0.2}Cu_{0.2}Zn_{0.2}O$ was ultrafast synthesized by the Joule heating technique within 3 seconds and was applied to LIBs for the first time as a conversion-type anode material. The material exhibits excellent electrochemical performance and cycling stability.

A novel rock-salt structure high-entropy oxide $Fe_{0.2}Co_{0.2}Ni_{0.2}Cu_{0.2}Zn_{0.2}O$ as a highly reversible lithium storage material

Xiaobin He[1], Xuemei Zeng[1], Wei Wang[1], Yaqing Guo[1], Shengjie Zheng[1], Yun Li[1], Guixing Mo[1], Jiatong Zhang[1], Shur Wang[1], Hao Wang[2](✉), and Yifei Yuan[1](✉)

[1] *College of Chemistry and Materials Engineering, Wenzhou University, Wenzhou 325035, China*
[2] *Centre for Future Materials, University of Southern Queensland, Springfield, QLD 4300, Australia*

Received: 14 May 2025; **Revised:** 3 July 2025; **Accepted:** 9 July 2025

✉Address correspondence to Hao Wang, Hao.Wang@unisq.edu.au; Yifei Yuan, yifeiyuan@wzu.edu.cn

Cite this article: *Nano Research*, 2025, 18, 94907784. https://doi.org/10.26599/NR.2025.94907784

ABSTRACT

High-entropy oxides (HEOs) composed of multiple metal elements have garnered significant attention as anode materials for lithium-ion batteries (LIBs), owing to their synergistic effects between constituent metal oxides and broad material design flexibility. However, the advancement of HEOs in LIBs has been hindered by time-consuming synthesis methods, complex fabrication procedures, and an insufficient understanding of their lithium storage mechanisms. In this study, a rock-salt structure HEO $Fe_{0.2}Co_{0.2}Ni_{0.2}Cu_{0.2}Zn_{0.2}O$ was ultrafast synthesized by the Joule heating technique within 3 seconds and was applied to LIBs for the first time as a conversion-type anode material. The material exhibits not only excellent capacity retention but also remarkable structural reversibility. Specifically, the reversible capacity is determined to be 1310 mAh g^{-1} for 200 cycles at 0.1 A g^{-1}, and 705 mAh g^{-1} for 3000 cycles at 5 A g^{-1}. Detailed mechanistic investigations reveal that ZnO serves as an electrochemically inactive structural stabilizer that maintains the rock-salt framework, while Cu^{2+} is difficult to oxidize back to its original state once reduced to Cu^0. This study provides critical insights into the composition-structure-property relationships of HEOs, offering valuable guidance for designing high-performance LIBs anode materials through entropy engineering.

KEYWORDS

high-entropy oxides, lithium-ion batteries, Joule heating, ultrafast synthesized

1 Instruction

Lithium-ion batteries (LIBs) have emerged as one of the most widely used energy storage solutions globally due to their efficiency and reliability. They are extensively applied in electric vehicles, energy storage systems, and portable electronic devices [1-6]. However, the currently commercially used intercalation anode materials, such as graphite and lithium titanate, have relatively low energy densities, which do not meet the increasing demand for higher energy density for energy storage [7-9]. Although silicon-based anode materials offer high energy densities, they suffer significant volume expansion, which requires further research and development to overcome [10-12]. Conversion-type transition metal oxides (TMOs) not only exhibit higher theoretical specific capacity compared to traditional graphite anode materials, but also demonstrate smaller volume expansion and better cycling stability than silicon anode materials. These advantages make them a highly promising next generation anode materials for LIBs [13, 14]. However, TMOs also experience substantial volume expansion and contraction during charging-discharging cycles, causing electrode material cracking. This damage leads to the detachment of active material from the current collector and imposes stress on the solid electrolyte interphase (SEI), resulting in continuous SEI growth and capacity degradation during cycling [15-20]. To address these critical issues, it is necessary to develop high-entropy oxides anode materials with better energy storage performance.

By adjusting the stoichiometric ratios and types of doped cations, high-entropy materials demonstrate exceptional compositional flexibility, which typically endows them with novel and unexpected physicochemical properties. Consequently, these materials have found wide-ranging applications in numerous fields, including superionic conductors, catalysts, thermoelectric materials, and battery electrodes [21-24]. Recently, high-entropy oxides (HEOs) inspired by the principle of high configurational entropy stability have gained attention as promising anode materials for LIBs [25-29]. HEOs are composed of five or more metal elements (each with 5-35% molar concentration) to achieve high configurational entropy (i.e., $S_{\mathrm{config}} \geq 1.5$ R) and are synthesized into a single-phase crystalline structure. Compared to single TMOs, HEOs exhibit highly uniform chemical composition and complex crystal structures with excellent structural stability. The synergistic effects among multiple elements further enhance the electrochemical performance of the materials [30-34]. HEOs have been studied by various scholars since the concept of entropy-stabilized was first proposed by Rost et al. in 2015 [35-40]. From the $Mg_{0.2}Co_{0.2}Ni_{0.2}Cu_{0.2}Zn_{0.2}O$ rock-salt structure reported by Sarkar et al. with a specific capacity of 600 mAh g^{-1} after 300 cycles at 0.2 A g^{-1} to the $(FeCoNiCrMn)_3O_4$ spinel structure reported by Liang's team with 611 mAh g^{-1} after 800 cycles at 3 A g^{-1} [37, 41], further proving the exceptional cycling stability of HEO. Despite these advances, the practical application of HEOs remains limited by high-energy synthesis methods and insufficient mechanistic understanding of their lithium storage behavior, highlighting the need for rapid synthesis methods and in-depth electrochemical characterization [42-47].

In this work, we report the ultrafast synthesis [48] of entropy-stabilized rock-salt structure $Fe_{0.2}Co_{0.2}Ni_{0.2}Cu_{0.2}Zn_{0.2}O$ via Joule heating in just 3 seconds. The morphology, microstructure, valence state, and electrochemical charge-discharge performance of HEO have been systematically investigated, comparing its electrochemical performance to TMOs. The reversible capacity is 1310 mAh g^{-1} for 200 cycles at 0.1 A g^{-1}, and the capacity at a relatively high current density of 5 A g^{-1} is also maintained at about 705 mAh g^{-1} after 3000 cycles, with a capacity retention of 87.16%. In-depth analysis using electrochemical *in-situ* X-ray diffraction (XRD), X-ray photoelectron spectroscopy (XPS), *ex-situ* and *in-situ* transmission electron microscopy (TEM) revealed the mechanisms of the reversible lithium storage performance in HEO. It was found that for $Fe_{0.2}Co_{0.2}Ni_{0.2}Cu_{0.2}Zn_{0.2}O$, ZnO was electrochemically inactive and acted as a structural pillar to maintain the rock-salt structure in the form of Zn^{2+} during cycling, allowing for a highly reversible rock-salt structure. While Fe, Co, and Ni serve as the primary contributors to the capacity. Additionally, Cu, presenting as Cu^0 after initial cycling, enhances electron conductivity and improves performance. The findings from this study offer valuable insights into the structural and compositional design of next generation HEOs electrode materials for advanced LIBs.

2 Material and Methods

2.1 Material synthesis

First, equimolar proportions of Fe_3O_4 (Mreda, 99%), CoO (Aladdin, 99.9%), NiO (Aladdin, 99.9%), CuO (Meryer, 99.5%) and ZnO (Aladdin, 99.8%) were added to a zirconia mixing vessel and mixed with stainless steel pellets in a ball mill at 400 revolutions per minute (rpm) for 4 hours. Then, the mixed powders were divided into portions of 0.35 grams each and compressed into small discs with a diameter of 1.5 cm under a pressure of 8 MPa using a hydraulic press. Graphite flakes were used as a support and conductor during the Joule sintering process to ensure uniform heating. A layered assembly was constructed by sandwiching the precursor pellet between two alumina flakes, which was then positioned centrally within a graphite flake stack and capped with an additional graphite flake. The samples were then rapidly heated to 1350 K for 3 seconds in an argon atmosphere heating chamber, followed by rapid cooling to room temperature. The entire process was completed within 10 seconds. Finally, the sintered HEO was pulverized in a quartz crucible to reduce particle size, preparing it for the subsequent cell electrodes preparation.

2.2 Material Characterizations

The crystal structure of the samples was characterized using XRD (Bruker D8 Advance with Cu Kα X-ray source) at 40 kV and 40 mA, over a 2θ range of 20º to 80º. The constituents of the samples were quantified by inductively coupled plasma optical emission spectroscopy (ICP-OES, PE Optima 8000). Microstructural analysis was conducted using transmission electron microscope (TEM, JEM-2100F with 200 kV acceleration voltage) and scanning electron microscope (SEM, Nova 200 Nano SEM with 15 kV acceleration voltage). The SEM samples were prepared by drying and dispersing on silicon wafers, while TEM samples were prepared by ultrasonic drying and dispersing on molybdenum grids. Energy-dispersive X-ray spectroscopy (EDS) and selected-area electron diffraction (SAED) were used to investigate the microstructure, chemical composition, and crystal structure of the materials. Additionally, X-ray photoelectron spectroscopy (XPS, PHI5000 VP III, K-alpha) was employed to analyze the valence states of the samples, with all spectra calibrated using the C 1s peak (C-C bond) at 284.8 eV as a reference.

2.3 Electrochemical Measurements

The electrochemical performance of the HEO anode was evaluated using CR2032 button half-cells. To prepare the electrode slurry the synthesized HEO powder, Ketjen Black conductive carbon, and sodium alginate binder were mixed in deionized water at a weight ratio of 7:2:1, followed by ball milling at 2000 rpm for 10 minutes. The resulting homogeneous slurry was uniformly coated onto a copper foil current collector and dried at 80℃ for 12 hours in a vacuum oven. The dried electrodes were punched into 12 mm diameter discs, with an active material mass loading of approximately 1.0 mg cm^{-2}, as measured by an analytical balance. The electrolyte consisted of 1 M $LiPF_6$ dissolved in a 1:1:1 (v/v) mixture of ethylene carbonate (EC), dimethyl carbonate (DMC), and diethyl carbonate (DEC). 75 µL of the electrolyte volume was used in each cell. A Whatman GF/D glass fiber separator was employed in the cell assembly, which was conducted in an argon-filled glove box (Mikrouna Super 1200, $H_2O/O_2 < 0.1$ ppm). For construction of a HEO//$LiNi_{0.8}Co_{0.1}Mn_{0.1}O_2$ full cell, an anode-to-cathode capacity ratio of 1.12 was used. The HEO anode was preconditioned and lithiated in a half cell prior to the full cell assembly. Cyclic voltammetry (CV) measurements were performed on a CHI 760E electrochemical workstation within a voltage window of 0.01-3.00 V (vs. Li^+/Li). Galvanostatic charge-discharge cycling and rate capability tests were carried out using a Neware CT-4008 battery tester over the voltage range of 0.01-3.00 V (vs. Li^+/Li). For post-cycling characterization, the cycled cells were disassembled in the glove box, followed by rinsing the electrodes with DMC to remove residual electrolyte. The cleaned electrodes were then dried under an inert atmosphere for 24 hours before further analysis.

3 Results and Discussion

Figure 1(a) illustrates the temperature profile of the Joule-heating ultrafast synthesis for HEO. The sample achieved rapid heating to 1350 K within 3 seconds followed by immediate cooling to room temperature, demonstrating exceptional process efficiency. Pre-sintering measurements revealed a sample diameter of 1.5 cm, which contracted to 1.3 cm after sintering, confirming enhanced material densification during thermal processing. Structural characterization of the synthesized material was subsequently conducted. The XRD pattern in Fig. 1(b) exhibits distinct diffraction peaks at 2θ = 36.59º, 42.50º, 61.67º, 73.89º and 77.78º, corresponding to the (111), (200), (220), (311), and (222) crystallographic planes of a cubic rock-salt structure, respectively. Calculated lattice spacings for these planes are 0.245 nm, 0.213 nm, 0.150 nm, 0.128 nm, and 0.122 nm, consistent with the $Fm\bar{3}m$ space group (PDF#74-2392). As illustrated in the inset of Fig. 1(b), the ball-and-stick model depicts the atomic configuration of the

HEO, where oxygen anions (red spheres) occupy fixed lattice sites, while five metal cations (green spheres) randomly distribute across cation sites with equal probability. This atomic disorder generates a high configurational entropy (S_{config}) of 1.61 R, calculated via Eq. (S1) in the ESM. According to high-entropy design criteria ($S_{\mathrm{config}} \geq 1.5$ R), this material qualifies as a high-entropy oxide [35].

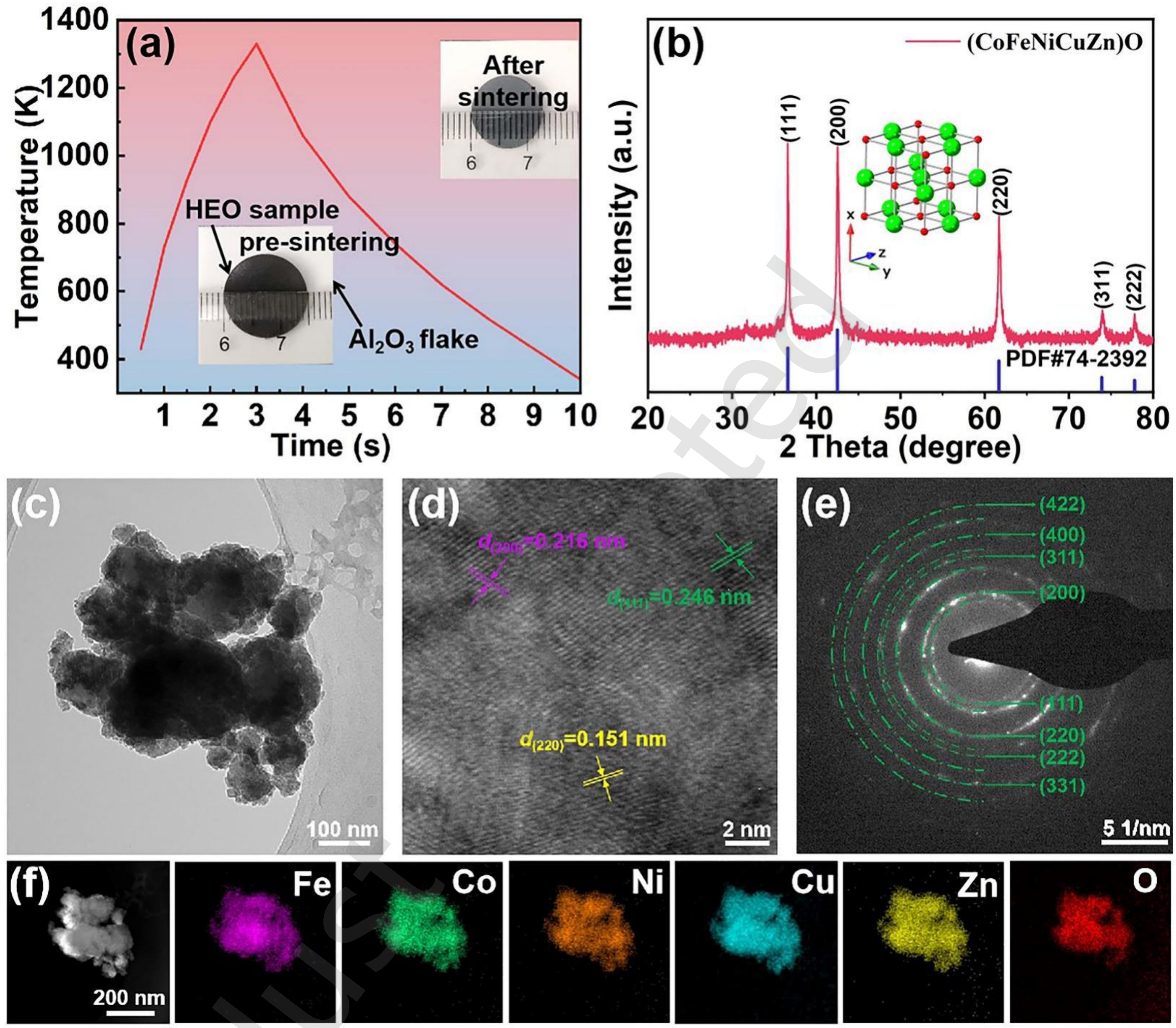

Figure 1 Structural characterization of HEO material. (**a**) Synthesis of rock-salt HEO by Joule heating. (b) XRD pattern of HEO and crystal model of rock-salt structure. The red spheres represent anion sites occupied by oxygen ions and the green spheres represent cation sites randomly occupied by five metal cations with equal probability. (c) TEM image and (d) HRTEM image of HEO. (e) SAED pattern of the polycrystalline structure of HEO. (f) HAADF image and EDS elemental mappings of HEO.

The structural characteristics of the HEO were systematically investigated through multi-scale electron microscopy analysis. The scanning electron microscope (SEM) image of HEO (Fig. S1 in the ESM) reveals a granular morphology with an average particle size of 143.13 nm. The TEM image observations in Fig. 1(c) demonstrate that larger HEO particles comprise randomly oriented sub-micron crystallites, as evidenced by distinct diffraction contrast variations. High-resolution TEM (HRTEM) image (Fig. 1(d)) resolves atomic lattice fringes with spacings of 0.246 nm, 0.216 nm, and 0.151 nm, corresponding to the (111), (200), and (220) planes of the rock-salt structure, respectively. By analyzing the selected-area electron diffraction (SAED) pattern of HEO (Fig. 1(e)), more profound comprehension of its crystal structure has been obtained. As shown in the figure, the distinct diffraction rings of HEO indicate a well-defined crystalline structure. The concentric diffraction rings correspond to eight crystallographic planes: $d_{(111)}$ = 0.246 nm, $d_{(200)}$ = 0.216 nm, $d_{(220)}$ = 0.151 nm, $d_{(311)}$ = 0.128 nm, $d_{(222)}$ = 0.123 nm, $d_{(400)}$ = 0.106 nm, $d_{(331)}$ = 0.098 nm, and $d_{(422)}$ = 0.087 nm. Furthermore, elemental analyses of HEO particles are performed using transmission electron microscopy (TEM) combined with energy-dispersive X-ray spectroscopy (EDS). The high-angle annular dark field (HAADF) image as well as the EDS elemental mappings show a homogeneous distribution of the elements Fe, Co, Ni, Cu, Zn, and O without any observable elemental segregation in Fig. 1(f). Quantitative analysis via inductively coupled plasma optical emission spectrometer (ICP-OES) and EDS (Table S1and Fig. S2 in the ESM) confirms near equal-molar metal ratios. The atomic ratios of Fe, Co, Ni, Cu, and Zn are close to 1:1:1:1:1. The amalgamation of the aforementioned analyses indicates the successful preparation of $Fe_{0.2}Co_{0.2}Ni_{0.2}Cu_{0.2}Zn_{0.2}O$ HEO material with a single-phase rock-salt structure.

The electrochemical performance of the rock-salt structure $Fe_{0.2}Co_{0.2}Ni_{0.2}Cu_{0.2}Zn_{0.2}O$ HEO was evaluated in CR2032 button cells with lithium metal as the counter electrode. Figure 2(a) presents the first three cyclic voltammetry (CV) cycles of the HEO anode with a scan rate of 0.1 mV s^{-1} and a voltage window of 0.01-3.0 V (vs. Li^+/Li). During the initial cathodic scan (lithiation), three distinct reduction peaks are observed at ≈ 1.51, 1.07, and 0.76 V, corresponding to the multi-step lithiation process of transition metal oxides. The subsequent anodic scan (delithiation) reveals two oxidation peaks at 1.67 V and 2.33 V, indicating metal nanoparticle (NP) re-oxidation. Notably, the near-perfect overlap of the second and third CV cycles demonstrates exceptional electrochemical reversibility after solid electrolyte interphase (SEI) stabilization. A characteristic cathodic peak shift from 0.76 V (first cycle) to 0.95 V (subsequent cycles) is attributed to irreversible SEI formation and electrolyte decomposition during initial activation, consistent with prior reports on conversion-type anodes [49, 50]. To further elucidate the reaction kinetics, the capacitive contribution to the total capacity was quantified through Trasatti analysis of CV data acquired at different scan rates (0.1-1.0 mV s^{-1}, Fig. S3 in the ESM). The theoretical capacity of this HEO, calculated using Eq. (S2) in the ESM, is 737.9 mAh g^{-1}. The actual capacity of this anode material in LIBs exceeds the theoretical capacity because the specific capacity of HEO originates from both capacitive-controlled contribution and diffusion-controlled contribution. The pseudocapacitance performance ratio of HEO in LIBs is shown in Fig. S3 in the ESM. The high specific capacity of HEO is partly attributed to pseudocapacitance performance (capacitive-controlled contribution) as the surface or near-surface regions of HEO can adsorb ions, thereby enabling significantly enhanced capacitive performance. Therefore, the HEO exhibits an exceptionally high specific capacity in LIBs.

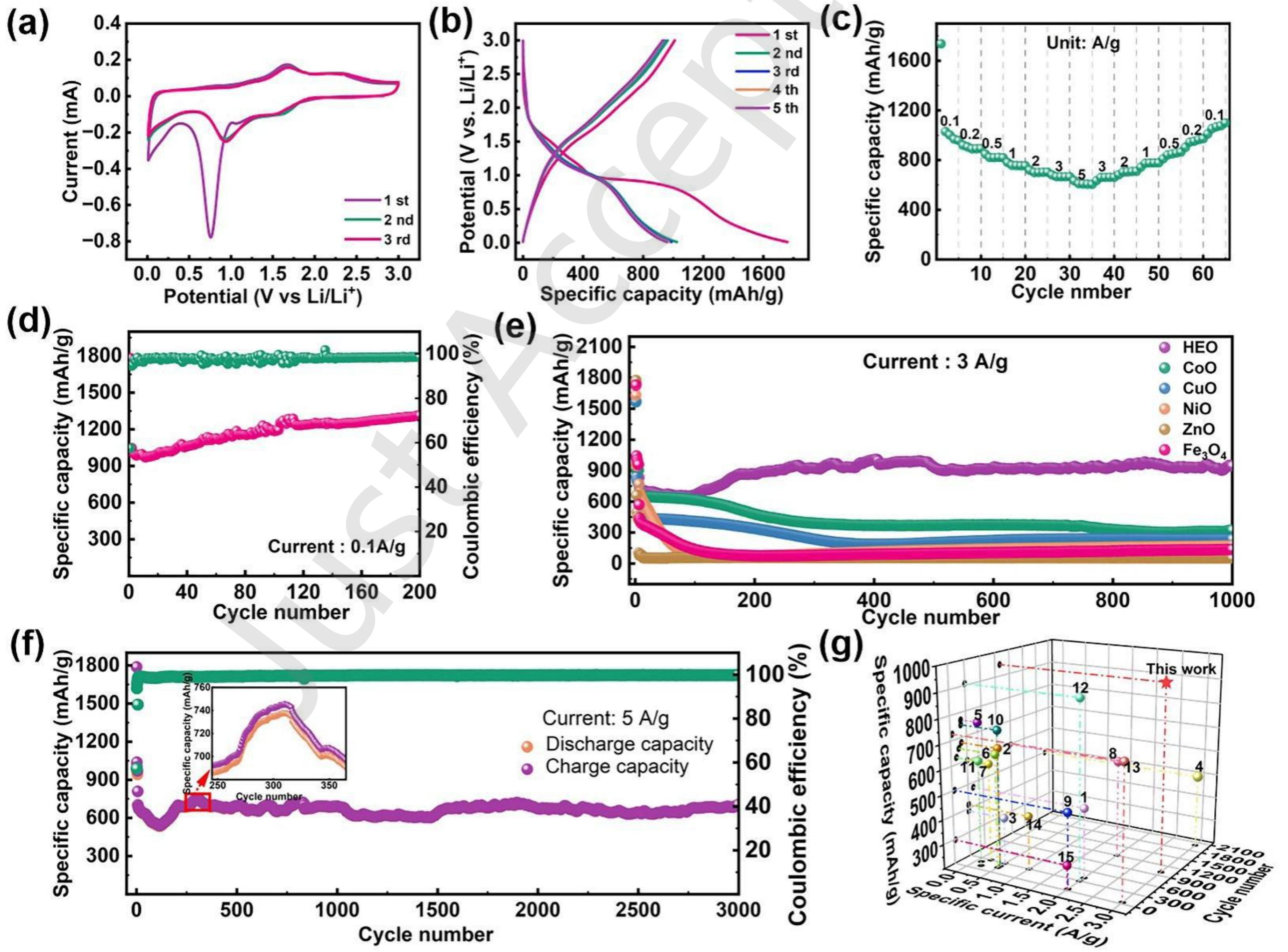

Figure 2 Energy storage performance of HEO anode characterized in half-cells. (a) The CV curves of HEO at 0.1 mV s^{-1} in the voltage range of 0.01-3.00 V. (b) Charge-discharge curves for the first 5 cycles at 0.1 A g^{-1}. (c) Rate performance at various current densities from 0.1 to 5 A g^{-1}. (d) Cycling stability of HEO at 0.1 A g^{-1}. (e) Performance comparison between HEO and TMOs at 3 A g^{-1}. (f) Long-term cycling performance of HEO at 5 A g^{-1}. (g) Electrochemical performance comparison of HEO with other reported HEO-based anodes.

Galvanostatic charge-discharge cycling was performed to evaluate the lithium storage performance of the HEO anode. As shown in Fig. 2(b), the first five cycles at 100 mA g^{-1} exhibit voltage plateaus aligning with CV-derived redox potentials (Fig.

2(a)). The initial discharge-charge capacities reached 1759 mAh g^{-1} and 1010 mAh g^{-1}, respectively, yielding the initial Coulombic efficiency (ICE) of 57.42%. This phenomenon is primarily attributed to the irreversible reactions of the electrode materials, the decomposition of the electrolyte, and the formation of the SEI. However, the discharge-charge performance becomes stable after the first cycle, further reflecting its good electrode reaction reversibility. To assess the performance of HEO at different discharge-charge rates, rate capability tests were conducted, as shown in Fig. 2(c). Specific capacities of 960, 894, 820, 755, 704, 667, and 606 mAh g^{-1} are maintained at progressively increased current densities of 0.1, 0.2, 0.5, 1, 2, 3, and 5 A g^{-1}, respectively. Rate capability tests reveal exceptional current tolerance of $Fe_{0.2}Co_{0.2}Ni_{0.2}Cu_{0.2}Zn_{0.2}O$. Notably, the HEO anode exhibits a unique capacity activation behavior, with gradual capacity increase during prolonged cycling. This trend is further corroborated by long-term cycling tests (Fig. 2(d)), where the capacity rises to 1315 mAh g^{-1} after 200 cycles at 0.1 A g^{-1} with 98.55% CE, demonstrating a long activation process and excellent capacity retention. The extra capacity beyond the redox reaction may arise from interfacial charge storage derived from the large active surface and surface defects, and/or the reversible conversion of the electrolyte surface layer catalyzed by the nanometallic particles [51].

To investigate whether the prolonged activation behavior observed in the HEO represents a universal characteristic of TMOs, comparative electrochemical evaluations were performed on five individual TMOs (CoO, CuO, NiO, ZnO, Fe_3O_4) and the HEO at 3 A g^{-1}. As shown in Fig. 2(e), traditional TMOs exhibit monotonically decaying capacity profiles, which stand in sharp contrast to the unique three-stage behavior of the HEO. Quantitative analysis after 1000 cycles reveals remarkable electrochemical performance of the HEO, delivering 947 mAh g^{-1} compared to 324 (CoO), 237 (CuO), 170 (NiO), 54 (ZnO), and 137 mAh g^{-1} (Fe_3O_4). Specific data can be found in Fig. S4 in the ESM. Particle size analysis of the six materials (Fig. S1 in the ESM) reveals that the average particle size of HEO is comparable to that of the TMOs. Thus, eliminating particle size effects as a performance determinant. Then, electrochemical impedance spectroscopy (EIS) analysis revealed that the HEO exhibits superior conductivity compared to TMOs (Fig. S5 in the ESM). Furthermore, galvanostatic intermittent titration technique (GITT) measurements comparing HEO with CoO (the best performing of the five TMOs) showed that HEO has a higher Li^+ diffusion coefficient (Fig. S6 in the ESM). Collectively, these properties contribute to the enhanced battery performance of HEO. As the cycle proceeds, the nanocrystals transform from large particles to clusters composed of smaller particles, generating abundant electrochemically active interfaces (Fig. S7 in the ESM). This structural transformation, coupled with the high-entropy "cocktail effect" (synergistic interactions between multimetallic constituents) collaboratively enhances both redox activity and structural integrity. The dual mechanisms explain the exceptional capacity retention and rate capability of the HEO. Furthermore, compared to the conventional time-consuming tube furnace synthesis method, the ultrafast synthesis approach is not only dramatically more time and labor efficient but also delivers significantly enhanced electrochemical performance (Fig. S8 in the ESM).

To further assess the ultra-long cycling stability of the HEO anode, cycling was performed at an ultrahigh current density of 5 A g^{-1} for 3000 cycles. As shown in Fig. 2(f), the HEO electrode delivers an exceptional reversible capacity of 705.6 mAh g^{-1} with near-ideal CE (99.8%). Excluding the initial five activation cycles at lower current density, the electrode demonstrates an outstanding capacity retention of 87.16%, which is better than most reported HEOs under comparable testing conditions. Compared with the results in previous reports, the HEO anode has a competitive electrochemical performance (Fig. 2(g)). Specific data can be found in Table S2 in the ESM [29, 36, 37, 49, 51-61]. This breakthrough performance originates from the synergistic interplay between entropy-stabilized structural integrity and nanoscale interfacial engineering, as elaborated in subsequent mechanistic analyses.

To elucidate the structural origin of the exceptional cycling stability in HEO anode, *in-situ* XRD analysis was performed during initial cycle. Figure 3 shows the *in-situ* XRD pattern of HEO, the HEO electrode maintains three characteristic rock-salt structure peaks corresponding to (111), (200), and (220) planes at 36.6º, 42.5º, and 61.7º, respectively. Notably, while these primary diffraction peaks experience significant intensity attenuation during lithiation, they persist throughout the electrochemical process. This behavior is consistent with the rock-salt structure $Mg_{0.2}Co_{0.2}Ni_{0.2}Cu_{0.2}Zn_{0.2}O$ reported previously [61]. Based on this, we speculate that in HEO, there are also some metal elements with lower electrochemical activity. These metal elements play an important role in maintaining the stability of the main framework. However, since the long-range lattice ordering of HEO is destroyed during the lithiation process, only short-range lattice ordering is left in the structure [37, 49, 62]. Due to the limitations of XRD characterization technique for amorphous structure analysis, subsequent nanoscale characterization was performed. We further conducted post-cycled TEM analysis on electrodes at fully lithiation (0.01 V vs. Li^+/Li) and delithiation (3.0 V) states.

The structural evolution of HEO after initial lithiation was investigated by TEM analysis, as shown in Figs. 4(a)-(e). Figure 4(a) shows the SAED pattern in which the diffraction intensities of the (111), (200), (220), (222), and (400) crystal planes of the original rock-salt structure was substantially weakened but not completely disappeared. While different diffraction rings were observed to be generated, distinct from those of the original rock-salt structure. Subsequently, the newly formed structures were preliminarily identified as metallic phases through HRTEM (Fig. 4(b)) and the corresponding fast Fourier transform (FFT). Figure 4(c) is an enlarged image of area Ⅰ in Fig. 4(b), corresponding to the retention of the retained rock-salt structure and Fig. 4(d) is an enlarged image of area Ⅱ in Fig. 4(b), corresponding to the formation of new phase metallic elemental structures. However, since the crystal spacing corresponding to the (111), (200) and (220) crystal planes of the Fe, Co, Ni and Cu metallic phases are between 0.203-0.211 nm, 0.174-0.183 nm and 0.123-0.129 nm, the lattice spacing of different elemental substances corresponding to the similar crystal plane results in difficulty in accurately determining which oxides have been reduced to metallic elements. Because the (111) and (200) crystal planes of Zn corresponding to 0.227 and 0.196 nm are not observed in SAED and HRTEM, the newly formed red diffraction rings after initial lithiation correspond to the phases of Fe/Co/Ni/Cu. The EDS elemental mappings (Fig. 4(e)) demonstrate homogeneous distribution of Fe, Co, Ni, Cu, Zn, and O without phase segregation. Quantitative EDS analysis (Fig. S9 in the ESM) confirms preserved near equal-molar metal ratios

(Fe:Co:Ni:Cu:Zn ≈ 1:1:1:1:1), indicating structural integrity of the high-entropy configuration after initial discharge. This atomic-scale homogeneity and dual-phase structural buffering enhance the exceptional cycling stability observed in electrochemical tests.

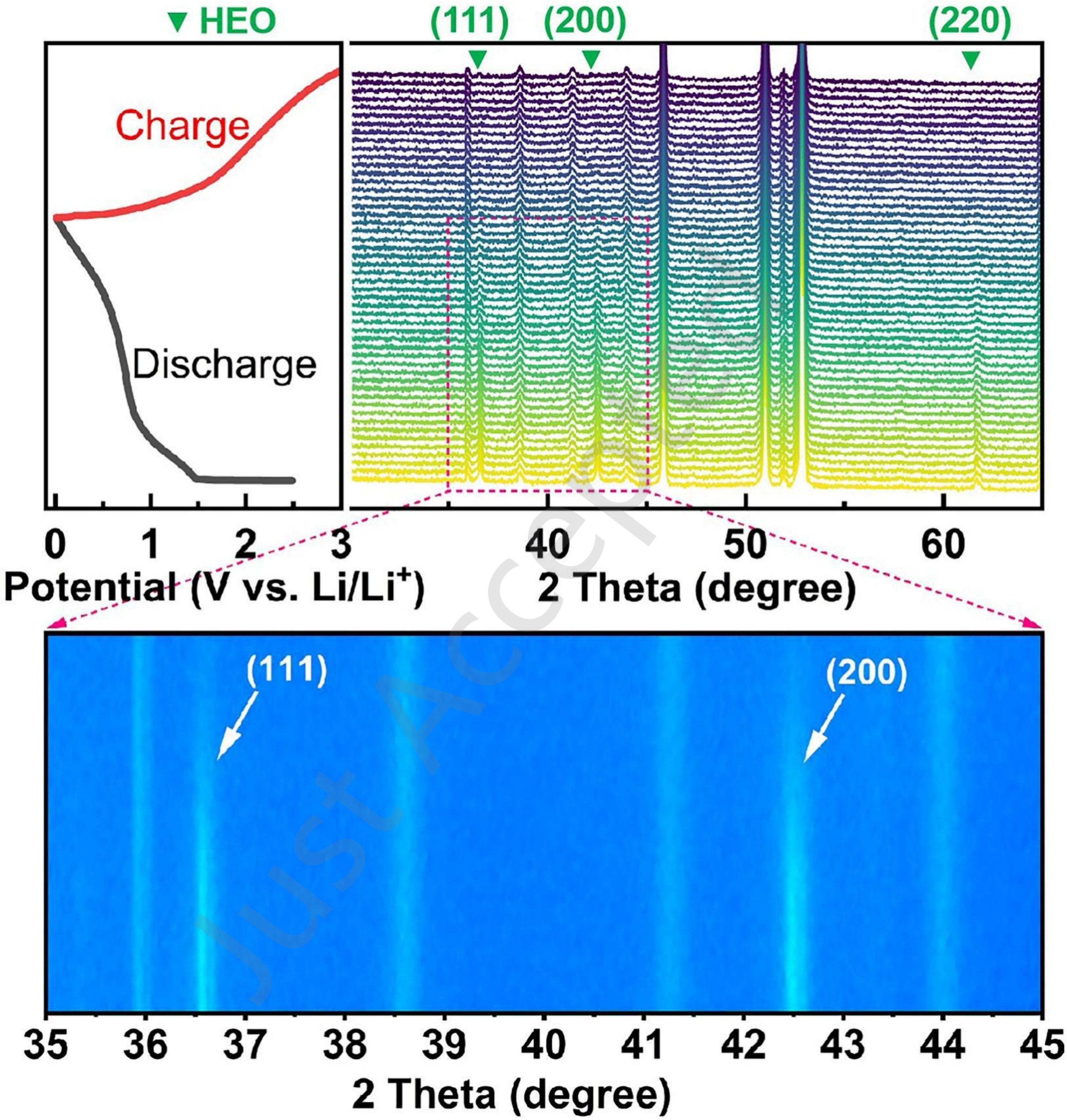

Figure 3 Electrochemical *in-situ* XRD patterns obtained during the discharge-charge process, with the corresponding potential curves shown on the left. The green triangles correspond to the characteristic diffraction peaks of HEO, while the other diffraction peaks are Be and BeO.

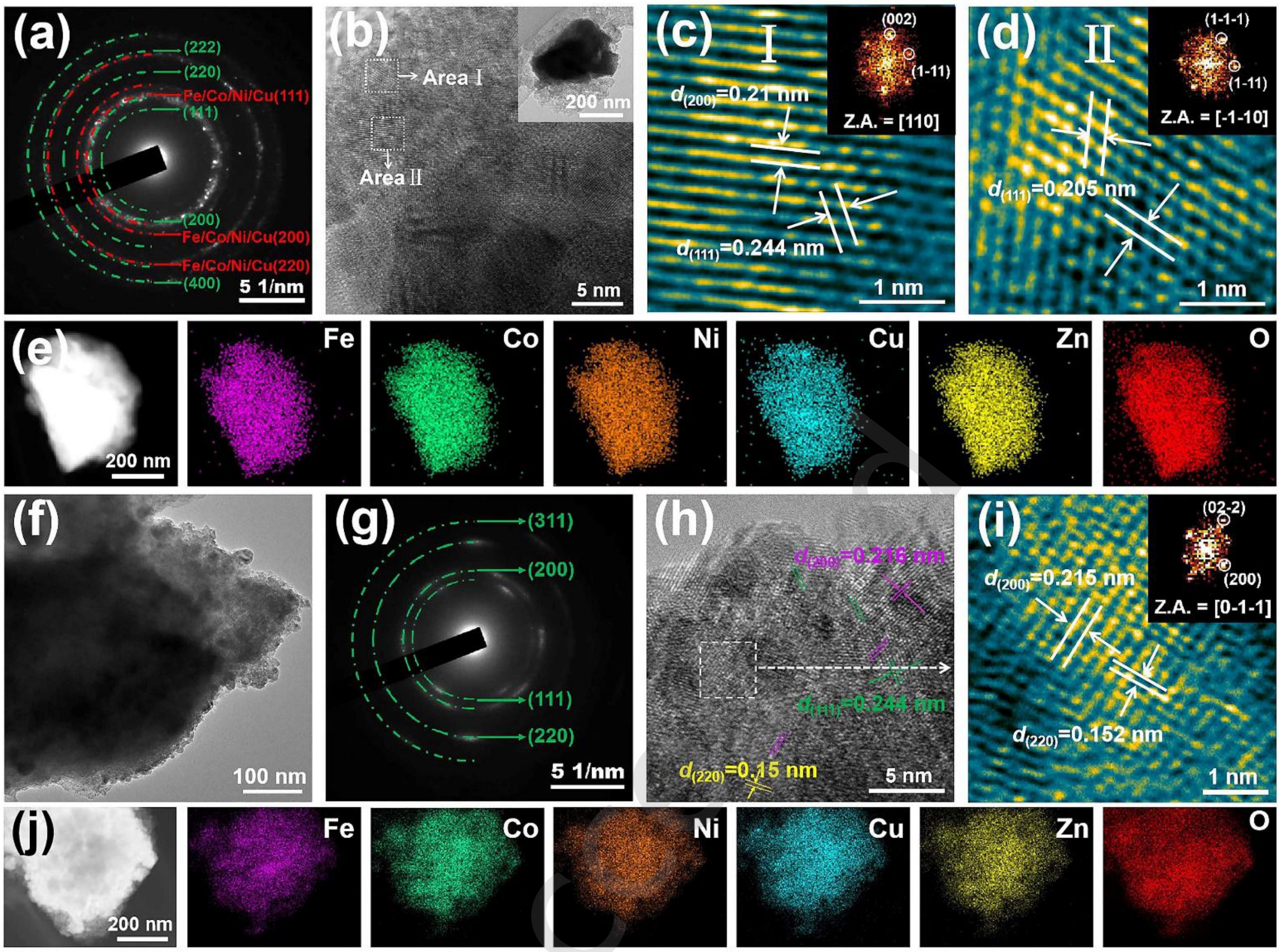

Figure 4 Reversible structure of HEO anode upon cycling. (a) SAED pattern of the first electrochemical lithiation. The rock-salt structure and new formed diffraction rings coexist in HEO after initial lithiation. (b) HRTEM image showing coexisting rock-salt structure and new phases in HEO after lithiation. (c) Enlarged HRTEM image of area Ⅰ in Fig. 4(b) and corresponding FFT pattern of the retained rock-salt structure. (d) Enlarged HRTEM of area Ⅱ in Fig. 4(b) and corresponding FFT pattern of metallic phase. (e) EDS elemental mappings of HEO anode after initial lithiation. (f) TEM image and (g) corresponding SAED pattern of HEO anode after initial cycle. (h-j) HRTEM images, corresponding FFT pattern and EDS elemental mappings after initial cycle.

To evaluate the structural reversibility of the HEO anode during electrochemical cycling, TEM characterization was performed (Figs. 4(f)-(j)). The SAED pattern and HRTEM images reveal well-defined lattice spacings of 0.244 nm, 0.216 nm, 0.150 nm, and 0.128 nm, confirming that the structure of the HEO is well recovered to the rock-salt structure after charge process. The EDS elemental mappings show that all elements show a homogeneous distribution, without detectable elemental segregation phenomenon. Quantitative elemental analysis provided in Fig. S10 in the ESM. The highly reversible crystal structure and excellent preservation of the uniform distribution of elements provide stable cycling performance for HEO anode.

To elucidate the lithium storage mechanism and identify the chemical state of formed metallic phases during cycling, X-ray photoelectron spectroscopy (XPS) was employed to analyze the valence state evolution of HEO in pristine, lithiation, and delithiation states. The XPS spectra of HEO, as shown in Fig. S11 in the ESM, clearly display the variation of characteristic peaks in different states. Specifically, in the Fe 2p spectra (Fig. 5(a)), HEO exhibits characteristic Fe $2p_{3/2}$ peaks at 710.65 eV (Fe^{2+}) and 712.53 eV (Fe^{3+}) in the pristine state, with corresponding Fe $2p_{1/2}$ peaks at 723.46 eV and 725.69 eV, respectively. The ratio of Fe^{2+}/Fe^{3+} is 63.35: 36.65. After discharging, Fe^{3+} is reduced to Fe^{2+} and Fe^0, the new peaks at 706.57 and 719.75 eV are related to Fe $2p_{3/2}$ and Fe $2p_{1/2}$ of Fe^0, with the ratio of Fe^{2+}/Fe^0 = 69.63: 30.37. After charging, Fe^0 is well restored to Fe^{2+} and Fe^{3+} with the ratio of Fe^{2+}/Fe^{3+} = 72.54: 27.46. In the Co 2p spectra (Fig. 5(b)), Co exists as Co^{2+} in the pristine state, with characteristic Co $2p_{3/2}$ and Co $2p_{1/2}$ peaks at 780.71 eV and 796.75 eV, respectively. New peaks at 778.18 eV and 793.3 eV corresponding to Co $2p_{3/2}$ and Co $2p_{1/2}$ peaks of Co^0 are observed after discharging, Co^{2+} is partially reduced to Co^0 with the ratio of Co^{2+}/Co^0 = 47.73: 52.27. Co could be fully restored to Co^{2+} after charging. In the Ni 2p spectra (Fig. 5(c)), Ni exists as Ni^{2+} in both pristine and delithiation states. The peak at 853.69 eV belongs to Ni $2p_{3/2}$ and the peak at 871.25 eV is attributed to Ni $2p_{1/2}$. After discharging, Ni^{2+} is completely reduced to Ni^0, as evidenced by the presence of Ni $2p_{3/2}$ and Ni $2p_{1/2}$ peaks at 852.55 eV and 869.91 eV. From Fig. 5(d), peaks at 934.51 eV and 954.24 eV correspond to Cu $2p_{3/2}$ and Cu $2p_{1/2}$ for Cu^{2+}. Cu exists as Cu^{2+} in the initial state. But in the discharged and charged states, only peaks at 932.60 eV and 952.57 eV are observed, which belong to Cu $2p_{3/2}$ and Cu $2p_{1/2}$ peaks of Cu^0. Cu element exists as

Cu^0 during cycling and is difficult to recover to Cu^{2+}. In the Zn 2p spectra (Fig. 5(e)), Zn persists as Zn^{2+} across all states, confirmed by photoelectron peaks at 1021.3 eV and 1044.55 eV and Auger peaks at 989.2 eV. The O 1s spectra in Fig. 5(f) is divided into three Gaussian peaks, namely lattice oxygen (O$_L$), oxygen vacancy (O$_V$), and surface chemisorbed oxygen (O$_C$) [63]. The O$_L$:O$_V$:O$_C$ ratios evolve from 30.28: 39.84: 29.88 (pristine) to 28.36: 35.27: 36.37 (lithiation) and 25.12: 48.31: 26.57 (delithiation). The presence of O$_V$ in electrode materials can significantly accelerate electron transport. They achieve this by reducing the charge transfer resistance and providing additional delocalized electrons, thereby increasing the density and mobility of charge carriers. This acceleration of electron transport, combined with the enhancement of configurational entropy, results in improved performance of the electrode materials in electrochemical reactions [64, 65].

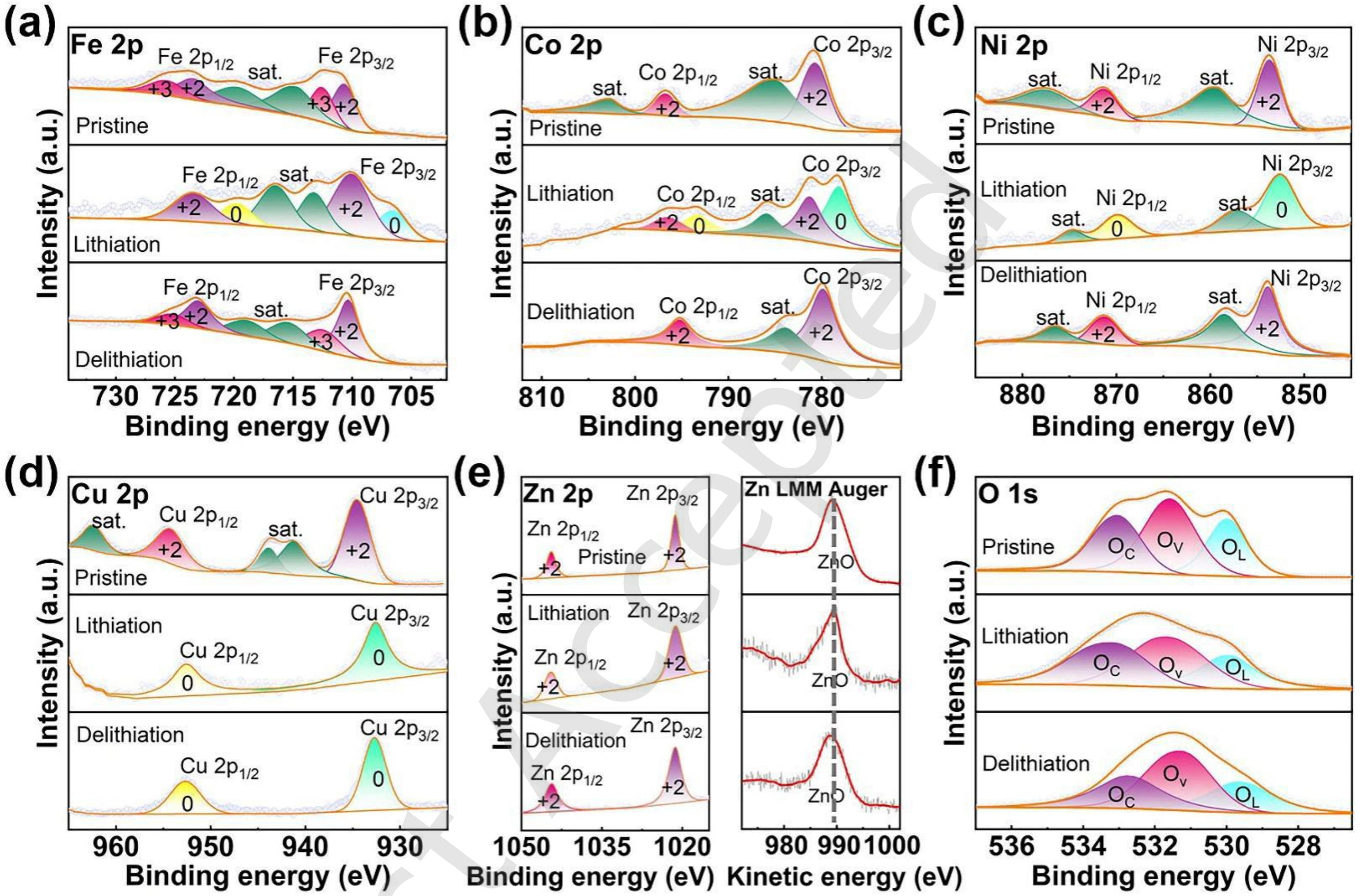

Figure 5 Chemical evolution of HEO in pristine, lithiation and delithiation states. XPS spectra of (a) Fe 2p, (b) Co 2p, (c) Ni 2p, (d) Cu 2p, (e) Zn 2p and Auger peaks, (f) O 1s.

XPS analysis reveals that the excellent structural reversibility of the HEO anode originates from two complementary mechanisms: structural stabilization by inactive components and kinetic enhancement through metallic conductivity pathways. Firstly, the electrochemical inactivity of ZnO, combined with the partial FeO and CoO, preserves the rock-salt framework throughout cycling. ZnO without participating in redox reactions, serving as a structural stabilizer that maintains long-range crystallographic order. This stabilization effect is further enhanced by FeO and CoO, which exhibit reversible phase transitions between their oxide and metallic states while retaining partial oxide character. Secondly, consistent with previous reports, CuO undergoes irreversible reduction to Cu^0 during the initial lithiation cycle. These metallic Cu domains form an interconnected conductive network that significantly enhances electron transport kinetics, creating "electron highways" throughout the electrode matrix. This conductive framework facilitates rapid lithium-ion storage kinetics while mitigating polarization losses during high-rate cycling [61, 65].

To verify that the Fe$_{0.2}$Co$_{0.2}$Ni$_{0.2}$Cu$_{0.2}$Zn$_{0.2}$O HEO not only has an excellent specific capacity but also achieves high reversibility of the rock-salt structure, TEM characterization was conducted on the sample after 1000 cycles. As shown in Fig. 6(a), the HEO particles maintain structural integrity without detectable crack and pulverization, as corroborated by SEM images during different cycles (Fig. S7 in the ESM). As shown in Figs. 6(b) and 6(c), the HRTEM and SAED results confirm the existence of rock-salt structure. The lattice spacings of 0.246, 0.21 and 0.15 nm are observed, which are attributed to (111), (200), and (220) diffraction rings of the rock-salt structure, respectively. The EDS elemental mappings (Fig. 6(d)) show a homogeneous distribution of the elements Fe, Co, Ni, Cu, Zn, and O without any observable elemental segregation, with near equal-molar metal ratios (1:1:1:1:1) quantified in Fig. S12 in the ESM. To further evaluate the stability of the HEO anode during multiple lithiation and delithiation cycles, we supplemented the study with *in-situ* TEM observations of initial three cycles lithiation and delithiation of the HEO. Figure S13 in the ESM displays the morphological changes of a single HEO NP over the initial three cycles, extracted from Movie S1 in the ESM. By alternately applying positive and negative bias to this NP with respect to the Li metal, the expansion and contraction processes of its projected area could be observed in real time. After the first full lithiation, the projected area of the NP increased by ≈ 36%. Following the first full delithiation, the projected area of the HEO decreased by ≈ 14% compared to the lithiated state,yet it still retained an expansion of ≈ 22% relative to its pristine state. This level of expansion is significantly lower than that observed in conventional TMOs [29, 61]. After three cycles, no obvious cracks or pulverization were observed in the NP, demonstrating that the HEO NP maintains excellent structural stability.

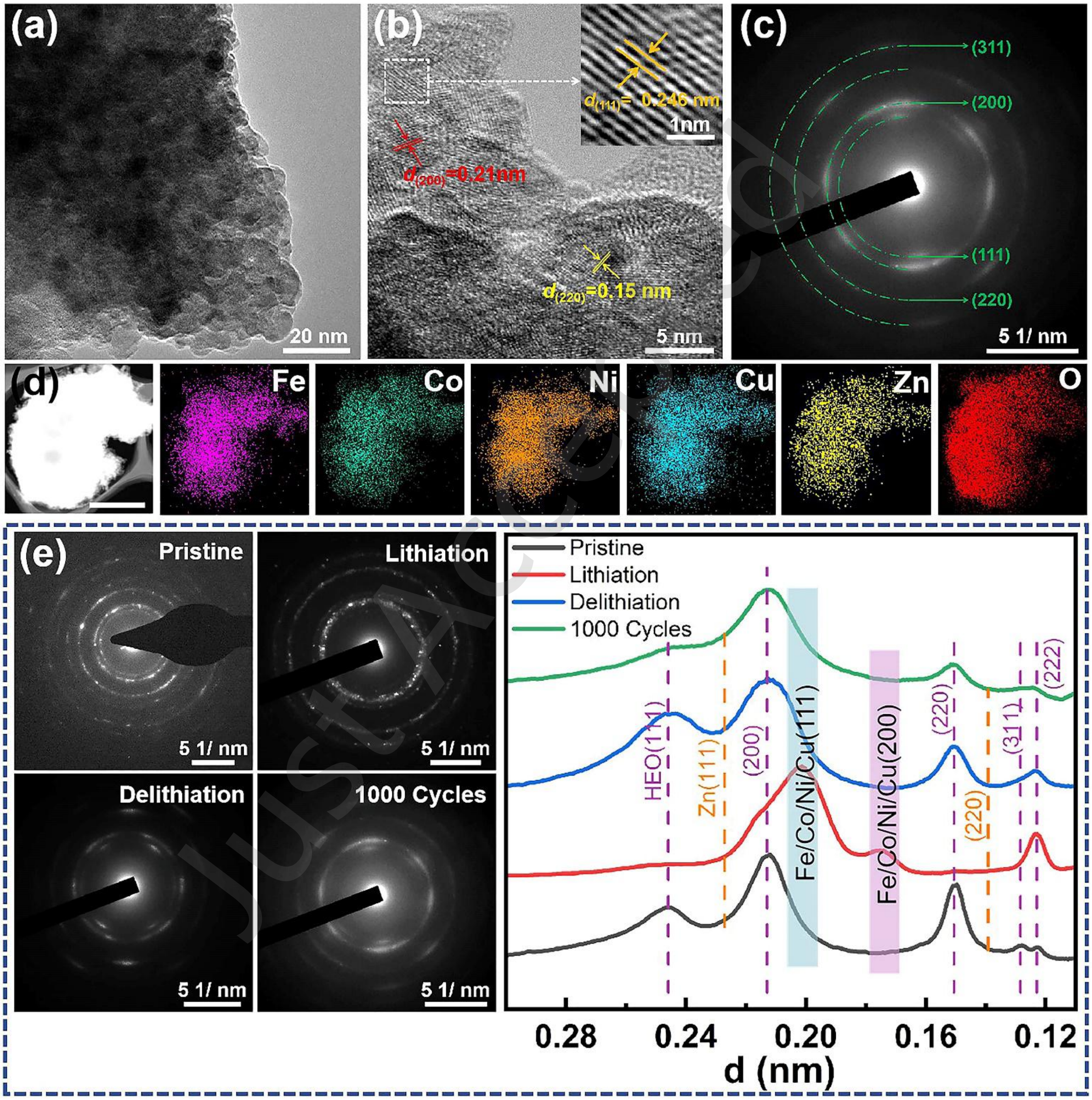

Figure 6 Stabilized structure of cycled HEO anode. (a-c) TEM, HRTEM and corresponding SAED results of HEO after 1000 cycles. The HEO particles maintain structural integrity without detectable crack and pulverization. (d) EDS elemental mappings of HEO after 1000 cycles. Scale bar, 300 nm. (e) The radially integrated intensity that corresponds to the SAED patterns exhibited in the four states. After discharging, the initial rock-salt structure is partially maintained, accompanied by emerged characteristic peaks of metallic Fe, Co, Ni, and Cu phases. After charging, the rock-salt structure is mostly recovered.

To demonstrate the highly reversible structure of HEO during cycling, radial intensity profiles were created from the SAED patterns of in the pristine, initial lithiation (0.01 V vs. Li^+/Li), initial delithiation (3.0 V vs. Li^+/Li), and after 1000 cycles (Charge to 3.0 V vs. Li^+/Li), as shown in Fig. 6(e). Notably, the presence of Zn^0 is not observed in any of the four states, indicating that zinc persists exclusively as Zn^{2+} throughout cycling and stabilizes the rock-salt framework. This functional element, including electrochemically inactive Zn, reversible Fe/Co/Ni and conductive Cu^0 provide a structural buffer and enhance electron/ion transport pathways during cycling. Together with the entropy-driven elemental homogeneity, the synergistic effect of these mechanisms provides outstanding electrochemical performance of HEO as an anode material in LIBs.

To evaluate the viability of HEO electrodes for practical battery applications, a HEO//$LiNi_{0.8}Co_{0.1}Mn_{0.1}O_2$ full cell was assembled (Fig. 7(a)). The charge-discharge profiles at various rates are shown in Fig. 7(b) (1 C = 275 mAh g^{-1} for the cathode). The HEO anode delivers a discharge specific capacity of 175 mAh g^{-1}at 0.1 C, which indicates that this HEO has great potential for use in LIBs.

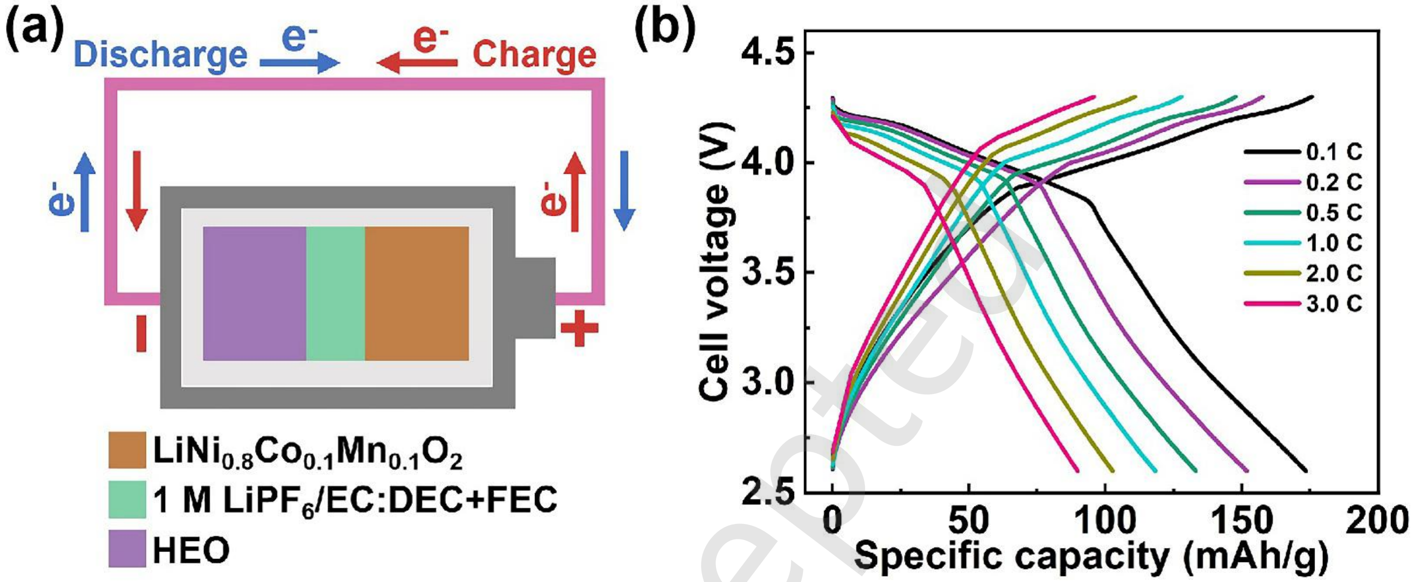

Figure 7 (a) Scheme of LIBs full cell with HEO anode and $LiNi_{0.8}Co_{0.1}Mn_{0.1}O_2$ cathode. (b) Charge-discharge profiles of HEO//$LiNi_{0.8}Co_{0.1}Mn_{0.1}O_2$ full cell measured at various rates.

4 Conclusion

In summary, the rock-salt structure $Fe_{0.2}Co_{0.2}Ni_{0.2}Cu_{0.2}Zn_{0.2}O$ HEO was successfully synthesized using ultrafast Joule heating technique within just 3 seconds and was applied to LIBs for the first time. The synthesized HEO demonstrated outstanding electrochemical performance, achieving a reversible capacity of 1310 mAh g^{-1} for 200 cycles at 0.1 A g^{-1} and 705 mAh g^{-1} for 3000 cycles at 5 A g^{-1}. The remarkable electrochemical performance is attributed to the excellent structural reversibility of the single-phase HEO achieved by this ultrafast synthesis method. Unlike conventionally synthesized HEOs, which often exhibit elemental phase segregation, this approach ensures atomic-scale elemental homogeneity. During cycling, the electrochemically inactive ZnO, along with partially FeO and CoO, helps preserve the rock-salt framework. This stabilization effect is further enhanced by the reversible phase transitions of FeO and CoO between their oxide and metallic states while retaining partial oxide character. Moreover, the irreversible reduction of Cu^{2+} to metallic Cu^0 establishes conductive network that facilitates rapid lithium-ion storage kinetics while mitigating polarization losses during high-rate cycling. The synergistic effect of these mechanisms contributes to the exceptional electrochemical performance of the HEO as an anode material in LIBs. This study provides valuable insight into the structural and compositional design of high-entropy materials and offers essential guidance for the development of new, general-purpose HEOs electrode materials in next generation long-life secondary batteries. The relevant details are shown below.

The optimization of next-generation HEOs materials can be achieved through element selection and compositional design. Utilizing electrochemically inert ZnO as a stable structural framework, leveraging the conductive network formed upon CuO reduction to metallic Cu, and incrementally increasing the proportion of active elements (Fe_3O_4, NiO, CoO, Cr_3O_4, etc.) via gradient doping can collectively enhance the electrochemical performance of HEOs in LIBs while maintaining structural stability. To address the issue of low ICE of the HEO, we plan to implement the following strategies to enhance ICE of HEOs electrode materials in future work: (Ⅰ) future efforts could focus on applying surface coatings to HEOs to further enhance lithium-ion diffusion coefficients and electrical conductivity, which would improve ICE, (Ⅱ) designing HEOs as a core-shell structure with an electrochemically inert outer shell may reduce contact between active material and electrolyte, thereby suppressing interfacial side reactions to enhance ICE, and (Ⅲ) tailoring the electrolyte composition by introducing advanced film-forming additives is expected to suppress electrolyte decomposition, thereby enhancing the ICE of HEOs electrode materials.

Electronic Supplementary Material: Supplementary material (additional testing and computational details, CV curves at various scan rates, Cycle performance of HEO and TMOs, EIS spectra of different electrodes, *in-situ* TEM of the HEO, XPS spectra and ICP-OES measured elemental ratios in HEO).

Acknowledgements

Declaration of competing interest

The authors declare that they have no known competing financial interests or personal relationships that could have appeared to influence the work reported in this paper.

References

[1] Chen, S.; Wang, Z.; Zhang, M.; Shi, X.; Wang, L.; An, W.; Li, Z.; Pan, F.; Yang, L. Practical evaluation of prelithiation strategies for next-generation lithium-ion batteries. *Carbon Energy*. **2023**, *5*, e323.

[2] Piątek, J.; Afyon, S.; Budnyak, T.M.; Budnyk, S.; Sipponen, M.H.; Slabon, A. Sustainable Li-ion batteries: chemistry and recycling. *Adv. Energy Mater*. **2021**, *11*, 2003456.

[3] Zhang, H.; Li, C.; Eshetu, G.G.; Laruelle, S.; Grugeon, S.; Zaghib, K.; Julien, C.; Mauger, A.; Guyomard, D.; Rojo, T., et al. From solid-solution electrodes and the rocking-chair concept to today's batteries. *Angew. Chem. Int. Ed*. **2020**, *59*, 534-538.

[4] Chayambuka, K.; Mulder, G.; Danilov, D.L.; Notten, P.H.L. From Li-ion batteries toward Na-ion chemistries: challenges and opportunities. *Adv. Energy Mater*. **2020**, *10*, 2001310.

[5] Zhang, H.; Hu, R.; Feng, S.; Lin, Z.; Zhu, M. SiO–Sn$_2$Fe@C composites with uniformly distributed Sn$_2$Fe nanoparticles as fast-charging anodes for lithium-ion batteries. *eScience*. **2023**, *3*, 100080.

[6] Guan, C.; Szeto, H.; Wander, O.; Kumar, V.; Clément, R.J.; Zhu, Y. Fast internal preheating of 4680 lithium-ion batteries in cold environments. *Nano Res*. **2024**, *17*, 8794-8802.

[7] Wu, P.; Xu, X.; Wu, Y.; Xu, F.; Wang, X.; Meng, J.; Han, C.; Liu, X.; Zhu, Z.; Mai, L. A stable CaV$_4$O$_9$ anode promises near-zero volume change and high-capacity lithium storage. *Adv. Energy Mater*. **2021**, *11*, 2003612.

[8] Wang, C.; Yang, C.; Zheng, Z. Toward practical high-energy and high-power lithium battery anodes: present and future. *Adv. Sci*. **2022**, *9*, 2105213.

[9] Kim, N.; Chae, S.; Ma, J.; Ko, M.; Cho, J. Fast-charging high-energy lithium-ion batteries via implantation of amorphous silicon nanolayer in edge-plane activated graphite anodes. *Nat. Commun*. **2017**, *8*, 812.

[10] Casimir, A.; Zhang, H.; Ogoke, O.; Amine, J.C.; Lu, J.; Wu, G. Silicon-based anodes for lithium-ion batteries: effectiveness of materials synthesis and electrode preparation. *Nano Energy*. **2016**, *27*, 359-376.

[11] Jiang, M.; Chen, J.; Zhang, Y.; Song, N.; Jiang, W.; Yang, J. Assembly: a key enabler for the construction of superior silicon-based anodes. *Adv. Sci*. **2022**, *9*, 2203162.

[12] Shen, J.; Zhang, S.; Wang, H.; Wang, R.; Hu, Y.; Mao, Y.; Wang, R.; Zhang, H.; Du, Y.; Fan, Y., et al. Unlocking the potential of silicon anodes in lithium-ion batteries: a claw-inspired binder with synergistic interface bonding. *eScience*. **2024**, *4*, 100207.

[13] Fang, S.; Bresser, D.; Passerini, S. Transition metal oxide anodes for electrochemical energy storage in lithium- and sodium-ion batteries. *Adv. Energy Mater*. **2019**, *10*, 1902485.

[14] Wu, W.; Wang, M.; Wang, J.; Wei, Z.; Zhang, T.; Chi, S.-S.; Wang, C.; Deng, Y. Transition metal oxides as lithium-free cathodes for solid-state lithium metal batteries. *Nano Energy*. **2020**, *74*, 104867.

[15] Du, W.; Zheng, Y.; Liu, X.; Cheng, J.; Chenna Krishna Reddy, R.; Zeb, A.; Lin, X.; Luo, Y. Oxygen-enriched vacancy spinel MFe$_2$O$_4$/carbon (M = Ni, Mn, Co) derived from metal-organic frameworks toward boosting lithium storage. *Chem. Eng. J*. **2023**, *451*, 138626.

[16] Chu, L.; Shi, Y.; Li, Z.; Sun, C.; Yan, H.; Ma, J.; Li, X.; Liu, C.; Gu, J.; Liu, K., et al. Solid electrolyte interphase on anodes in rechargeable lithium batteries. *Nano Res*. **2023**, *16*, 11589-11603.

[17] Esmaeilpour, M.; Jana, S.; Li, H.; Soleymanibrojeni, M.; Wenzel, W. A solution-mediated pathway for the growth of the solid electrolyte interphase in lithium-ion batteries. *Adv. Energy Mater*. **2023**, *13*, 2203966.

[18] Xu, X.; Liu, Y.; Kapitanova, O.O.; Song, Z.; Sun, J.; Xiong, S. Electro-chemo-mechanical failure of solid electrolytes induced by growth of internal lithium filaments. *Adv. Mater*. **2022**, *34*, 2207232.

[19] Lin, R.; He, Y.; Wang, C.; Zou, P.; Hu, E.; Yang, X.Q.; Xu, K.; Xin, H.L. Characterization of the structure and chemistry of the solid-electrolyte interface by cryo-EM leads to high-performance solid-state Li-metal batteries. *Nat. Nanotechnol*. **2022**, *17*, 768-776.

[20] Zhang, Z.; Li, Y.; Xu, R.; Zhou, W.; Li, Y.; Oyakhire, S.T.; Wu, Y.; Xu, J.; Wang, H.; Yu, Z., et al. Capturing the swelling of solid-electrolyte interphase in lithium metal batteries. *Science*. **2022**, *375*, 66-70.

[21] Sun, Y.; Wu, T.; Bao, Z.; Moon, J.; Huang, Z.; Chen, Z.; Chen, H.; Li, M.; Yang, Z.; Chi, M., et al. Defect engineering of ceria nanocrystals for enhanced catalysis via a high-entropy oxide strategy. *ACS Cent. Sci*. **2022**, *8*, 1081-1090.

[22] Huang, Z.; Wang, L.; Li, T.; Venkatraman, K.; He, Y.; Polo-Garzon, F.; Smith, J.; Du, Y.; Hu, L.; Wu, Z., et al. Atomic scale responses of high entropy oxides to redox environments. *Nano Lett*. **2024**, *24*, 11537-11543.

[23] Shahbazi, H.; Seraji, P.; Farraj, H.; Yang, T.; Kim, A.; Fattahpour, S.; Papailias, I.; Diamond, M.; Namvar, S.; Ahmadiparidari, A., et al. Resiliency, morphology, and entropic transformations in high-entropy oxide nanoribbons. *Science*. **2025**, *388*, 950-956.

[24] Liang, L.; Su, M.; Sun, Z.; Wang, L.; Hou, L.; Liu, H.; Zhang, Q.; Yuan, C. High-entropy doping promising ultrahigh-Ni Co-free single-crystalline cathode toward commercializable high-energy lithium-ion batteries. *Sci. Adv*. **2024**, *10*, eado4472.

[25] Lu, W.; Liebscher, C.H.; Dehm, G.; Raabe, D.; Li, Z. Bidirectional transformation enables hierarchical nanolaminate dual-phase high-entropy alloys. *Adv. Mater*. **2018**, *30*, 1804727.

[26] Skrabalak, S.E. Mashing up metals with carbothermal shock. *Science*. **2018**, *359*, 1467.

[27] Sarkar, A.; Wang, Q.; Schiele, A.; Chellali, M.R.; Bhattacharya, S.S.; Wang, D.; Brezesinski, T.; Hahn, H.; Velasco, L.; Breitung, B. High-entropy oxides: fundamental aspects and electrochemical properties. *Adv. Mater*. **2019**, *31*, 1806236.

[28] Joo, S.H.; Bae, J.W.; Park, W.Y.; Shimada, Y.; Wada, T.; Kim, H.S.; Takeuchi, A.; Konno, T.J.; Kato, H.; Okulov, I.V. Beating thermal coarsening in nanoporous materials via high-entropy design. *Adv. Mater*. **2020**, *32*, 1906160.

[29] Hou, S.; Su, L.; Wang, S.; Cui, Y.; Cao, J.; Min, H.; Bao, J.; Shen, Y.; Zhang, Q.; Sun, Z., et al. Unlocking the origins of highly reversible lithium storage and stable cycling in a spinel high-entropy oxide anode for lithium-ion batteries. *Adv. Funct. Mater*. **2023**, *34*, 2307923.

[30] Yao, L.; Zou, P.; Wang, C.; Jiang, J.; Ma, L.; Tan, S.; Beyer, K.A.; Xu, F.; Hu, E.; Xin, H.L. High-entropy and superstructure-stabilized layered oxide cathodes for sodium-ion batteries. *Adv. Energy Mater*. **2022**, *12*, 2201989.

[31] Akrami, S.; Murakami, Y.; Watanabe, M.; Ishihara, T.; Arita, M.; Fuji, M.; Edalati, K. Defective high-entropy oxide photocatalyst with high activity for CO$_2$ conversion. *Appl. Catal. B-Environ*. **2022**, *303*, 120896.

[32] Ding, F.; Ji, P.; Han, Z.; Hou, X.; Yang, Y.; Hu, Z.; Niu, Y.; Liu, Y.; Zhang, J.; Rong, X., et al. Tailoring planar strain for robust structural stability in high-entropy layered sodium oxide cathode materials. *Nat. Energy*. **2024**, *9*, 1529-1539.

[33] Han, L.; Zhu, S.; Rao, Z.; Scheu, C.; Ponge, D.; Ludwig, A.; Zhang, H.; Gutfleisch, O.; Hahn, H.; Li, Z., et al. Multifunctional high-entropy materials. *Nat. Rev. Mater*. **2024**, *9*, 846-865.

[34] Cai, T.; Cai, M.; Mu, J.; Zhao, S.; Bi, H.; Zhao, W.; Dong, W.; Huang, F. High-entropy layered oxide cathode enabling high-rate for solid-state sodium-ion batteries. *Nano-micro Lett*. **2023**, *16*, 10.

[35] Rost, C.M.; Sachet, E.; Borman, T.; Moballegh, A.; Dickey, E.C.; Hou, D.; Jones, J.L.; Curtarolo, S.; Maria, J.P. Entropy-stabilized oxides.

Nat. Commun. **2015**, *6*, 8485.

[36] Su, L.; Ren, J.; Lu, T.; Chen, K.; Ouyang, J.; Zhang, Y.; Zhu, X.; Wang, L.; Min, H.; Luo, W., et al. Deciphering structural origins of highly reversible lithium storage in high entropy oxides with in situ transmission electron microscopy. *Adv. Mater*. **2023**, *35*, 2205751.

[37] Sarkar, A.; Velasco, L.; Wang, D.; Wang, Q.; Talasila, G.; De Biasi, L.; Kubel, C.; Brezesinski, T.; Bhattacharya, S.S.; Hahn, H., et al. High entropy oxides for reversible energy storage. *Nat. Commun*. **2018**, *9*, 3400.

[38] Sun, S.; Dai, C.; Zhao, P.; Xi, S.; Ren, Y.; Tan, H.R.; Lim, P.C.; Lin, M.; Diao, C.; Zhang, D., et al. Spin-related Cu-Co pair to increase electrochemical ammonia generation on high-entropy oxides. *Nat. Commun*. **2024**, *15*, 260.

[39] Liu, F.; Yu, M.; Chen, X.; Li, J.; Liu, H.; Cheng, F. Defective high-entropy rocksalt oxide with enhanced metal–oxygen covalency for electrocatalytic oxygen evolution. *Chinese J. Catal*. **2022**, *43*, 122-129.

[40] Miao, L.; Sivak, J.T.; Kotsonis, G.; Ciston, J.; Ophus, C.L.; Dabo, I.; Maria, J.P.; Sinnott, S.B.; Alem, N. Chemical environment and structural variations in high entropy oxide thin film Probed with electron microscopy. *ACS. Nano*. **2024**, *18*, 14968-14977.

[41] Hong, C.; Tao, R.; Tan, S.; Pressley, L.A.; Bridges, C.A.; Li, H.Y.; Liu, X.; Li, H.; Li, J.; Yuan, H., et al. In situ cyclized polyacrylonitrile coating: key to stabilizing porous high‐entropy oxide anodes for high‐performance lithium‐ion batteries. *Adv. Funct. Mater*. **2024**, *35*, 2412177.

[42] Chen, H.; Lin, W.; Zhang, Z.; Jie, K.; Mullins, D.R.; Sang, X.; Yang, S.-Z.; Jafta, C.J.; Bridges, C.A.; Hu, X., et al. Mechanochemical synthesis of high entropy oxide materials under ambient conditions: dispersion of catalysts via entropy maximization. *ACS Mater. Lett*. **2019**, *1*, 83-88.

[43] Zhang, R.-Z.; Reece, M.J. Review of high entropy ceramics: design, synthesis, structure and properties. *J. Mater. Chem. A*. **2019**, *7*, 22148-22162.

[44] Usharani, N.J.; Bhandarkar, A.; Subramanian, S.; Bhattacharya, S.S. Antiferromagnetism in a nanocrystalline high entropy oxide (Co,Cu,Mg,Ni,Zn)O: magnetic constituents and surface anisotropy leading to lattice distortion. *Acta. Mater*. **2020**, *200*, 526-536.

[45] Trusov, G.V.; Tarasov, A.B.; Goodilin, E.A.; Rogachev, A.S.; Roslyakov, S.I.; Rouvimov, S.; Podbolotov, K.B.; Mukasyan, A.S. Spray solution combustion synthesis of metallic hollow microspheres. *J. Phys. Chem. C*. **2016**, *120*, 7165-7171.

[46] Wang, D.; Liu, Z.; Du, S.; Zhang, Y.; Li, H.; Xiao, Z.; Chen, W.; Chen, R.; Wang, Y.; Zou, Y., et al. Low-temperature synthesis of small-sized high-entropy oxides for water oxidation. *J. Mater. Chem. A*. **2019**, *7*, 24211-24216.

[47] Yu, L.; Zeng, K.; Li, C.; Lin, X.; Liu, H.; Shi, W.; Qiu, H.J.; Yuan, Y.; Yao, Y. High‐entropy alloy catalysts: From bulk to nano toward highly efficient carbon and nitrogen catalysis. *Carbon Energy*. **2022**, *4*, 731-761.

[48] Wang, C.; Ping, W.; Bai, Q.; Cui, H.; Hensleigh, R.; Wang, R.; Brozena, A.H.; Xu, Z.; Dai, J.; Pei, Y., et al. A general method to synthesize and sinter bulk ceramics in seconds. *Science*. **2020**, *368*, 521-526.

[49] Xiao, B.; Wu, G.; Wang, T.; Wei, Z.; Sui, Y.; Shen, B.; Qi, J.; Wei, F.; Zheng, J. High-entropy oxides as advanced anode materials for long-life lithium-ion batteries. *Nano Energy*. **2022**, *95*, 106962.

[50] Pu, X.; Zhao, D.; Fu, C.; Chen, Z.; Cao, S.; Wang, C.; Cao, Y. Understanding and calibration of charge storage mechanism in cyclic voltammetry curves. *Angew. Chem. Int. Ed*. **2021**, *60*, 21310-21318.

[51] Liu, X.; Yu, Y.; Li, K.; Li, Y.; Li, X.; Yuan, Z.; Li, H.; Zhang, H.; Gong, M.; Xia, W., et al. Intergrating hollow multishelled structure and high entropy engineering toward enhanced mechano-electrochemical properties in lithium battery. *Adv. Mater*. **2024**, *36*, 2312583.

[52] Patra, J.; Nguyen, T.X.; Tsai, C.C.; Clemens, O.; Li, J.; Pal, P.; Chan, W.K.; Lee, C.H.; Chen, H.Y.T.; Ting, J.M., et al. Effects of elemental modulation on phase purity and electrochemical properties of Co‐free high‐entropy spinel oxide anodes for lithium‐ion batteries. *Adv. Funct. Mater*. **2022**, *32*, 2110992.

[53] Nguyen, T.X.; Patra, J.; Tsai, C.C.; Xuan, W.Y.; Chen, H.Y.T.; Dyer, M.S.; Clemens, O.; Li, J.; Majumder, S.B.; Chang, J.K., et al. Secondary‐phase‐induced charge–discharge performance enhancement of Co‐free high entropy spinel oxide electrodes for Li‐ion batteries. *Adv. Funct. Mater*. **2023**, *33*, 2300509.

[54] Triolo, C.; Xu, W.; Petrovičovà, B.; Pinna, N.; Santangelo, S. Evaluation of entropy‐stabilized $(Mg_{0.2}Co_{0.2}Ni_{0.2}Cu_{0.2}Zn_{0.2})O$ oxides produced via solvothermal method or electrospinning as anodes in lithium‐ion batteries. *Adv. Funct. Mater*. **2022**, *32*, 2202892.

[55] Luo, X.F.; Patra, J.; Chuang, W.T.; Nguyen, T.X.; Ting, J.M.; Li, J.; Pao, C.W.; Chang, J.K. Charge-discharge mechanism of high-entropy Co-free spinel oxide toward Li^+ storage examined using operando quick-scanning X-ray absorption spectroscopy. *Adv. Sci*. **2022**, *9*, 2201219.

[56] Nguyen, T.X.; Patra, J.; Chang, J.-K.; Ting, J.-M. High entropy spinel oxide nanoparticles for superior lithiation–delithiation performance. *J. Mater. Chem. A*. **2020**, *8*, 18963-18973.

[57] Huang, C.-Y.; Huang, C.-W.; Wu, M.-C.; Patra, J.; Xuyen Nguyen, T.; Chang, M.-T.; Clemens, O.; Ting, J.-M.; Li, J.; Chang, J.-K., et al. Atomic-scale investigation of lithiation/delithiation mechanism in high-entropy spinel oxide with superior electrochemical performance. *Chem. Eng. J*. **2021**, *420*, 129838.

[58] Dong, Q.; Hong, M.; Gao, J.; Li, T.; Cui, M.; Li, S.; Qiao, H.; Brozena, A.H.; Yao, Y.; Wang, X., et al. Rapid synthesis of high-entropy oxide microparticles. *Small*. **2022**, *18*, 2104761.

[59] Wang, X.L.; Kim, E.M.; Senthamaraikannan, T.G.; Lim, D.-H.; Jeong, S.M. Porous hollow high entropy metal oxides $(NiCoCuFeMg)_3O_4$ nanofiber anode for high-performance lithium-ion batteries. *Chem. Eng. J*. **2024**, *484*, 149509.

[60] Liu, X.; Xing, Y.; Xu, K.; Zhang, H.; Gong, M.; Jia, Q.; Zhang, S.; Lei, W. Kinetically accelerated lithium storage in high-entropy (LiMgCoNiCuZn)O enabled by oxygen vacancies. *Small*. **2022**, *18*, 2200524.

[61] Wang, W.; Song, W.; Li, Y.; Guo, Y.; Yang, K.; Yu, L.; Xie, F.; Ren, Q.; He, K.; Wang, S., et al. Mesocrystallinely stabilized lithium storage in high-entropy oxides. *Nano Energy*. **2024**, *124*, 109482.

[62] Chen, S.; Bao, M.; Jia, Y.; Shao, X.; Guo, Y.; Li, S.; Mao, A.; Tan, J.; Liu, X. Lattice distortion induced rock salt high-entropy oxide for high-rate lithium-ion storage. *J. Alloys Compd*. **2024**, *990*, 174480.

[63] Lei, F.; Sun, Y.; Liu, K.; Gao, S.; Liang, L.; Pan, B.; Xie, Y. Oxygen vacancies confined in ultrathin indium oxide porous sheets for promoted visible-light water splitting. *J. Am. Chem. Soc*. **2014**, *136*, 6826-6829.

[64] Tang, L.; Yang, Y.; Guo, H.; Wang, Y.; Wang, M.; Liu, Z.; Yang, G.; Fu, X.; Luo, Y.; Jiang, C., et al. High configuration entropy activated lattice oxygen for O_2 formation on perovskite electrocatalyst. *Adv. Funct. Mater*. **2022**, *32*, 2112157.

[65] Wang, K.; Hua, W.; Huang, X.; Stenzel, D.; Wang, J.; Ding, Z.; Cui, Y.; Wang, Q.; Ehrenberg, H.; Breitung, B., et al. Synergy of cations in high entropy oxide lithium ion battery anode. *Nat. Commun*. **2023**, *14*, 1487.

Electronic Supplementary Material

A novel rock-salt structure high-entropy oxide $Fe_{0.2}Co_{0.2}Ni_{0.2}Cu_{0.2}Zn_{0.2}O$ as a highly reversible lithium storage material

Xiaobin He[1], Xuemei Zeng[1], Wei Wang[1], Yaqing Guo[1], Shengjie Zheng[1], Yun Li[1], Guixing Mo[1], Jiatong Zhang[1], Shun Wang[1], Hao Wang[2](✉), and Yifei Yuan[1](✉)

[1] *College of Chemistry and Materials Engineering, Wenzhou University, Wenzhou 325035, China*
[2] *Centre for Future Materials, University of Southern Queensland, Springfield, QLD 4300, Australia*

✉Address correspondence to Hao Wang, Hao.Wang@unisq.edu.au; Yifei Yuan, yifeiyuan@wzu.edu.cn

Supporting information to https://doi.org/10.26599/NR.2025.94907784

1. Supplementary Equations

Equation S1 Formula for calculating the entropy of a configuration, where x_i and x_j are the mole fractions of the elements present in the cation and anion sites respectively, and R is the universal gas constant. N and M are the number of anions and cations, respectively.

$$S = -R\left[\left(\sum_{i=1}^{N} x_i \ln x_i\right)_{\text{cation-site}} + \left(\sum_{j=1}^{M} x_j \ln x_j\right)_{\text{anion-site}}\right] \quad (S1)$$

Equation S2 Formula for calculating theoretical capacity, where n is the number of electrons transferred per molecule of active material, F is the Faraday constant, M is the molar mass of the active material, and 3.6 is the unit conversion factor.

$$C = \frac{nF}{3.6M} \quad (S2)$$

2. Supplementary Figures

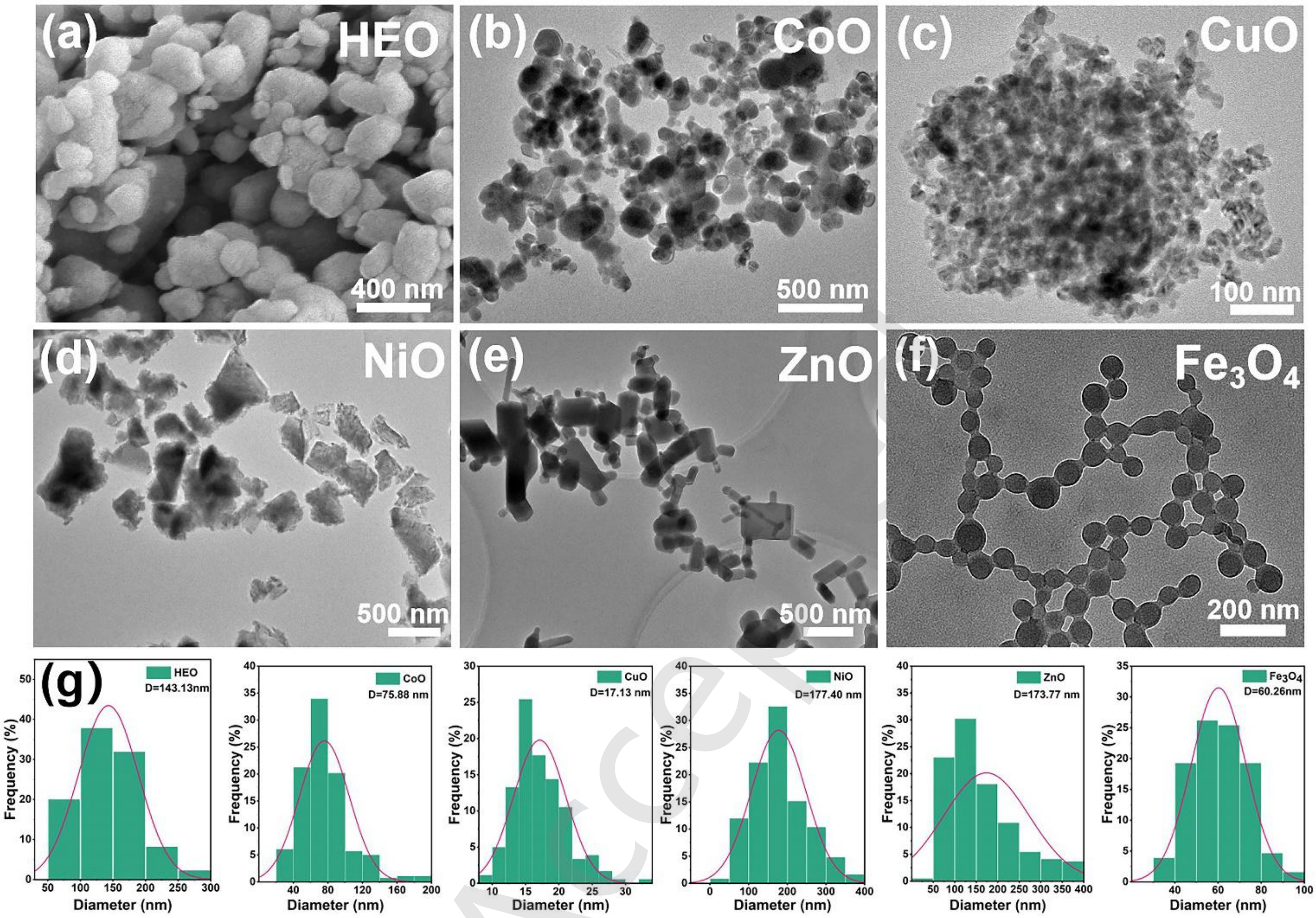

Figure S1 SEM image of (a) HEO. TEM images of (b) CoO. (c) CuO. (d) NiO. (e) ZnO and (f) Fe_3O_4. (g) The particle size distributions of HEO, CoO, CuO, NiO, ZnO and Fe_3O_4..

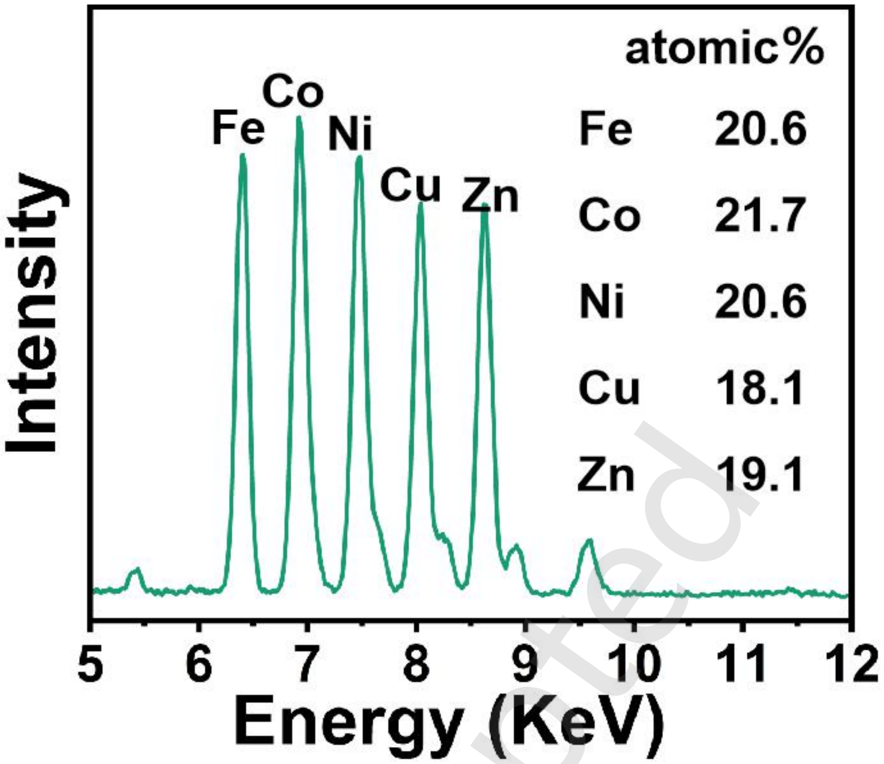

Figure S2 The intensity line plot and elemental scale analysis in STEM-EDS of initial HEO.

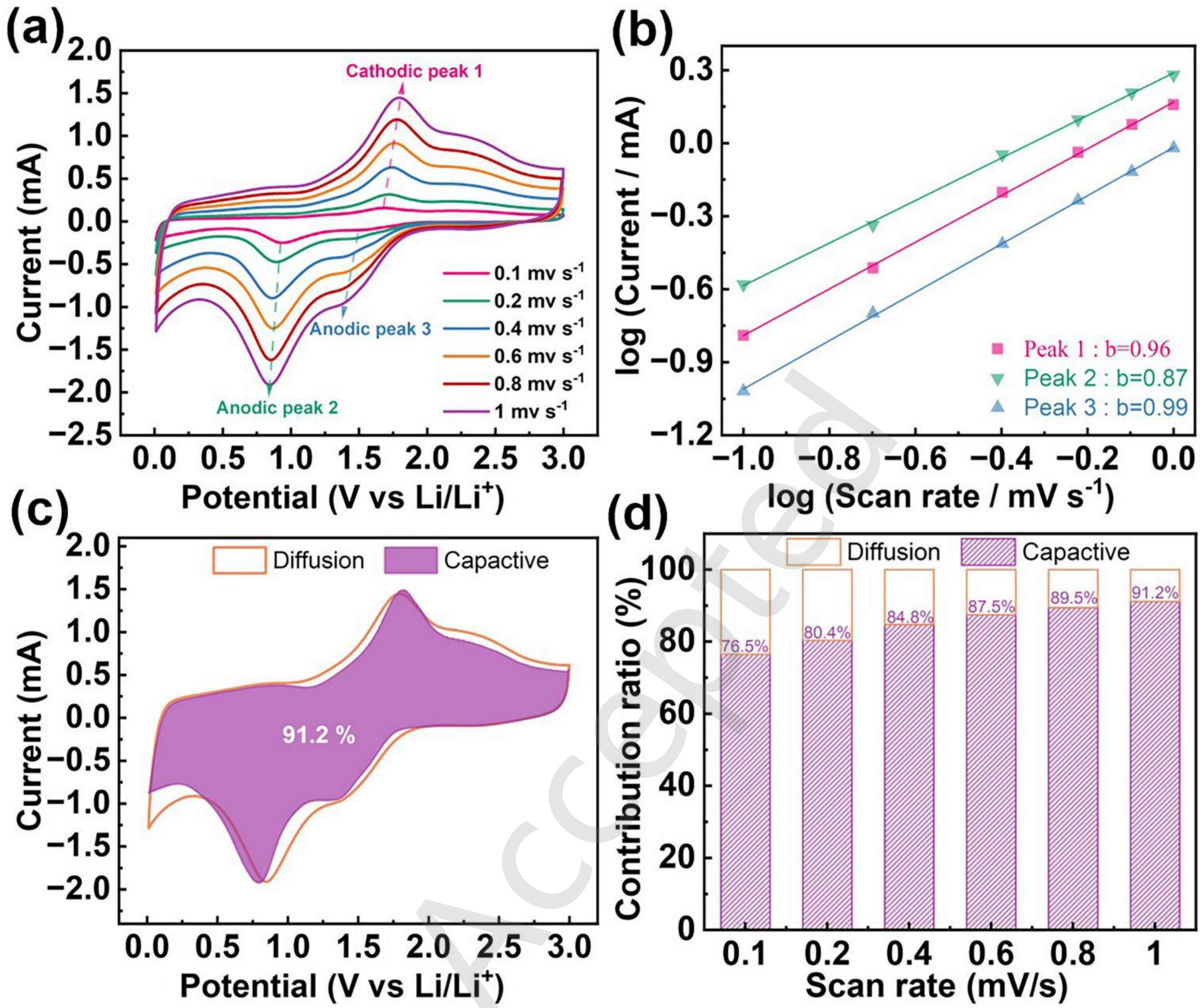

Figure S3 (a) CV curves at various scan rates of 0.1, 0.2, 0.4, 0.6, 0.8 and 1 mV s^{-1}. (b) Determination of the b value using the relationship between peak current and scan rate. (c) CV curve with separation between total current (solid line) and capacitive currents (shadow area) at 1 mV s^{-1}. (d) capacitive-controlled capacity contribution of HEO at various scan rates.

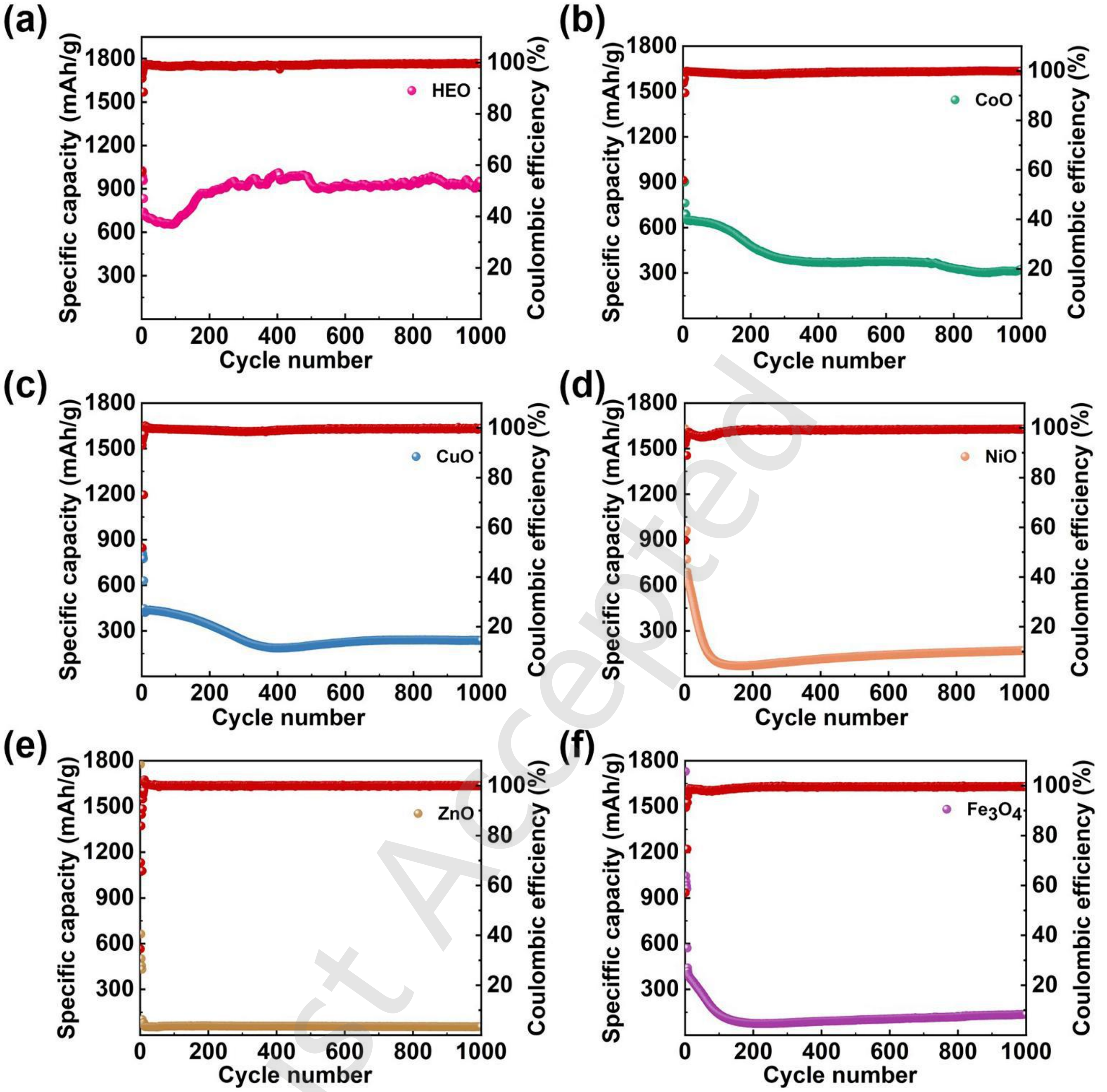

Figure S4 Cycle performance of (a) HEO. (b) CoO. (c) CuO. (d) NiO. (e) ZnO and (f) Fe_3O_4 at 1000 mA g^{-1} current, first activated at 100 mA g^{-1} current for five cycles.

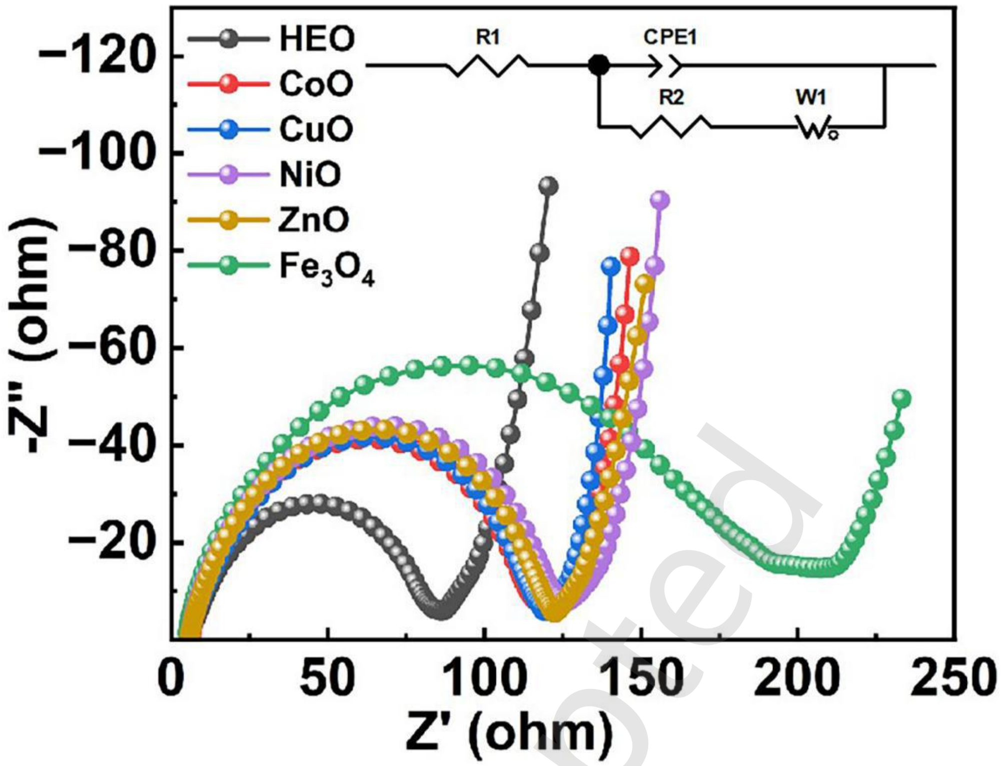

Figure S5 EIS spectra of different electrodes.

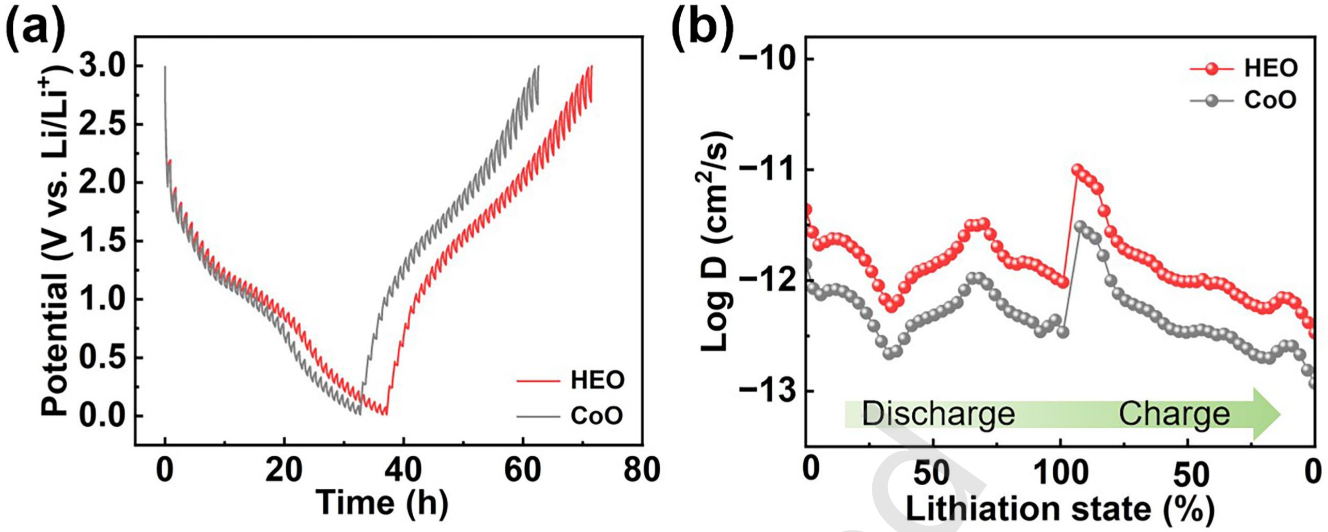

Figure S6 (a) GITT curves of HEO and CoO. (b) The calculated Li^+ diffusion coefficients of HEO and CoO.

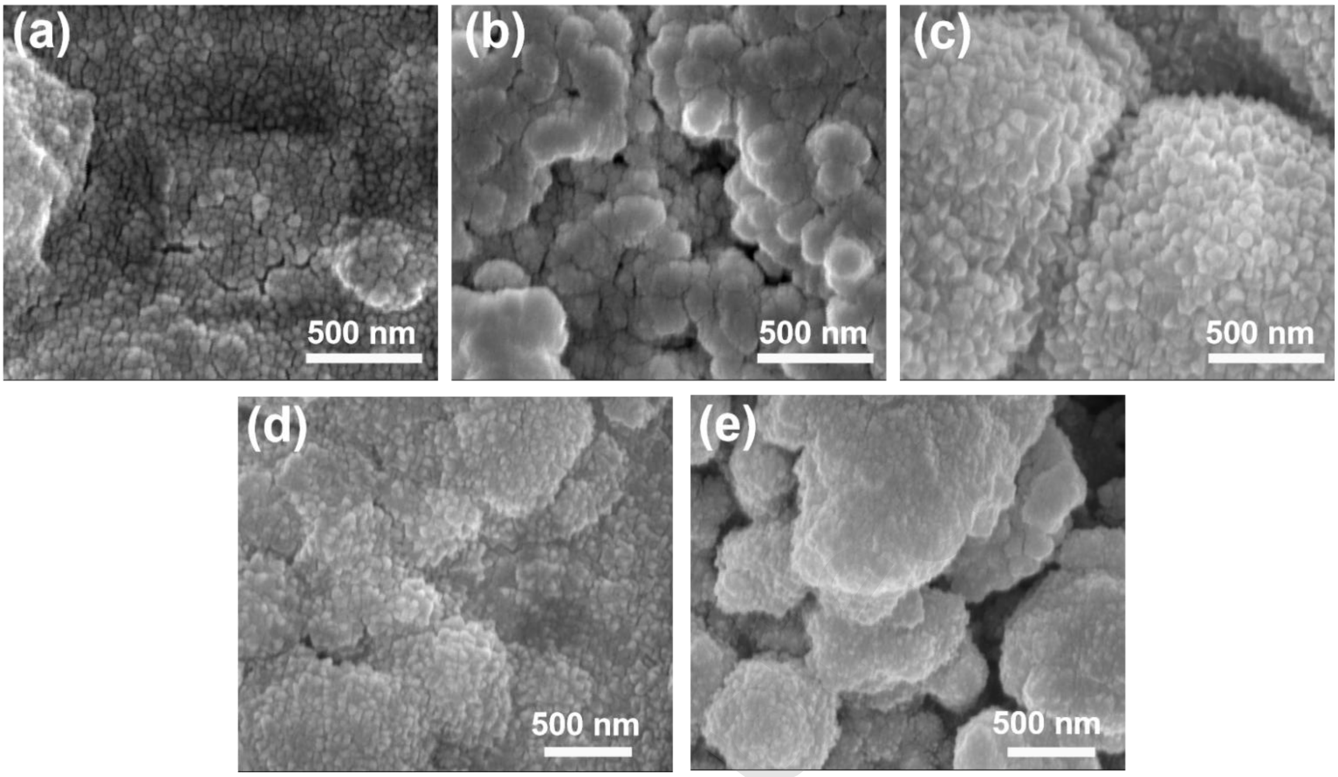

Figure S7 SEM images at different cycles. (a) 1 cycle. (b) 50 cycles. (c) 150 cycles. (d) 400 cycles. (e) 1000 cycles.

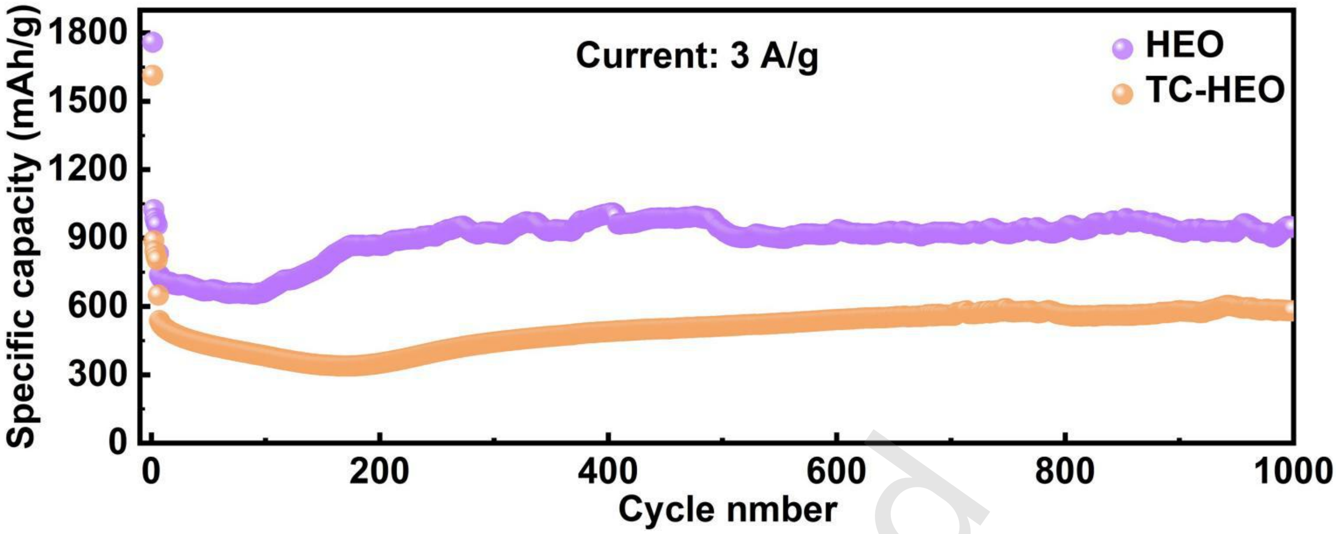

Figure S8 The electrochemical performance of ultrafast synthesized HEO and time-consuming synthesized HEO (TC-HEO) was compared at a current density of 3000 mA g^{-1}.

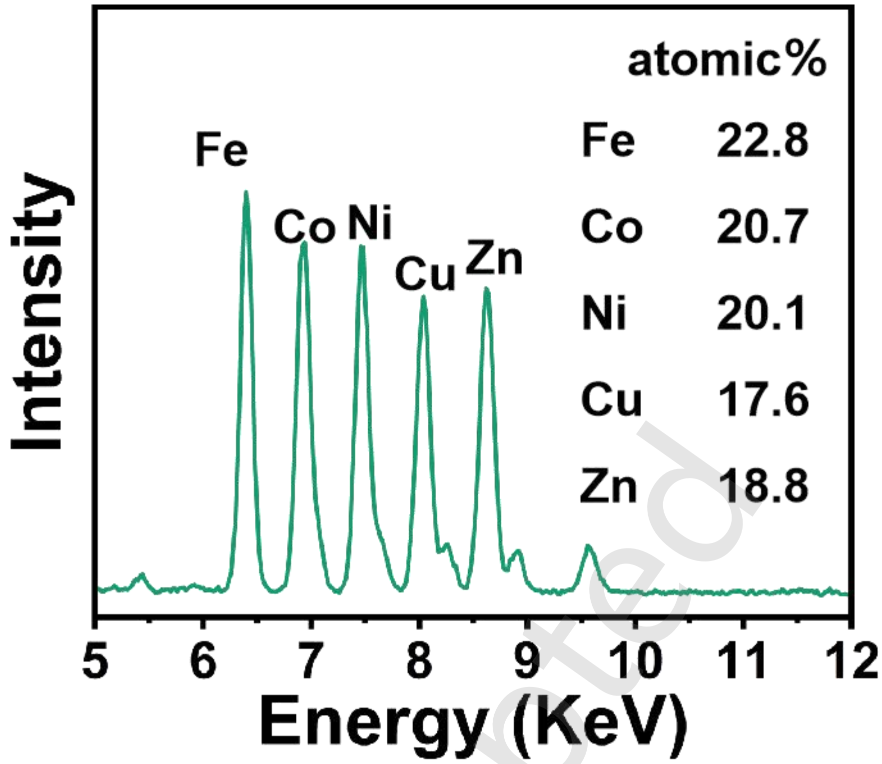

Figure S9 The intensity line plot and elemental scale analysis in STEM-EDS of HEO after lithiation.

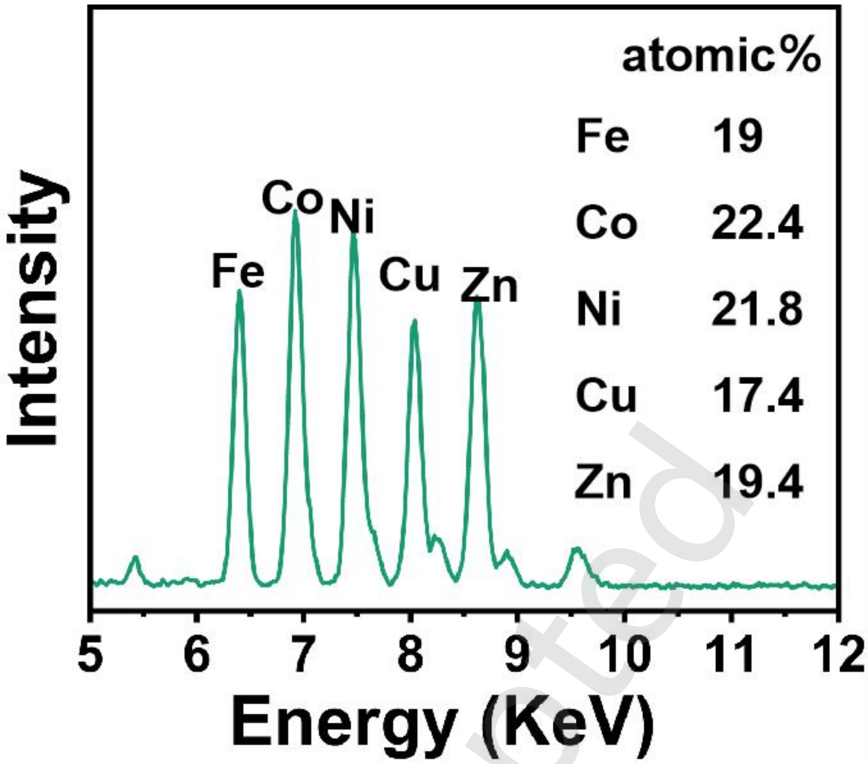

Figure S10 The intensity line plot and elemental scale analysis in STEM-EDS of HEO after delithiation.

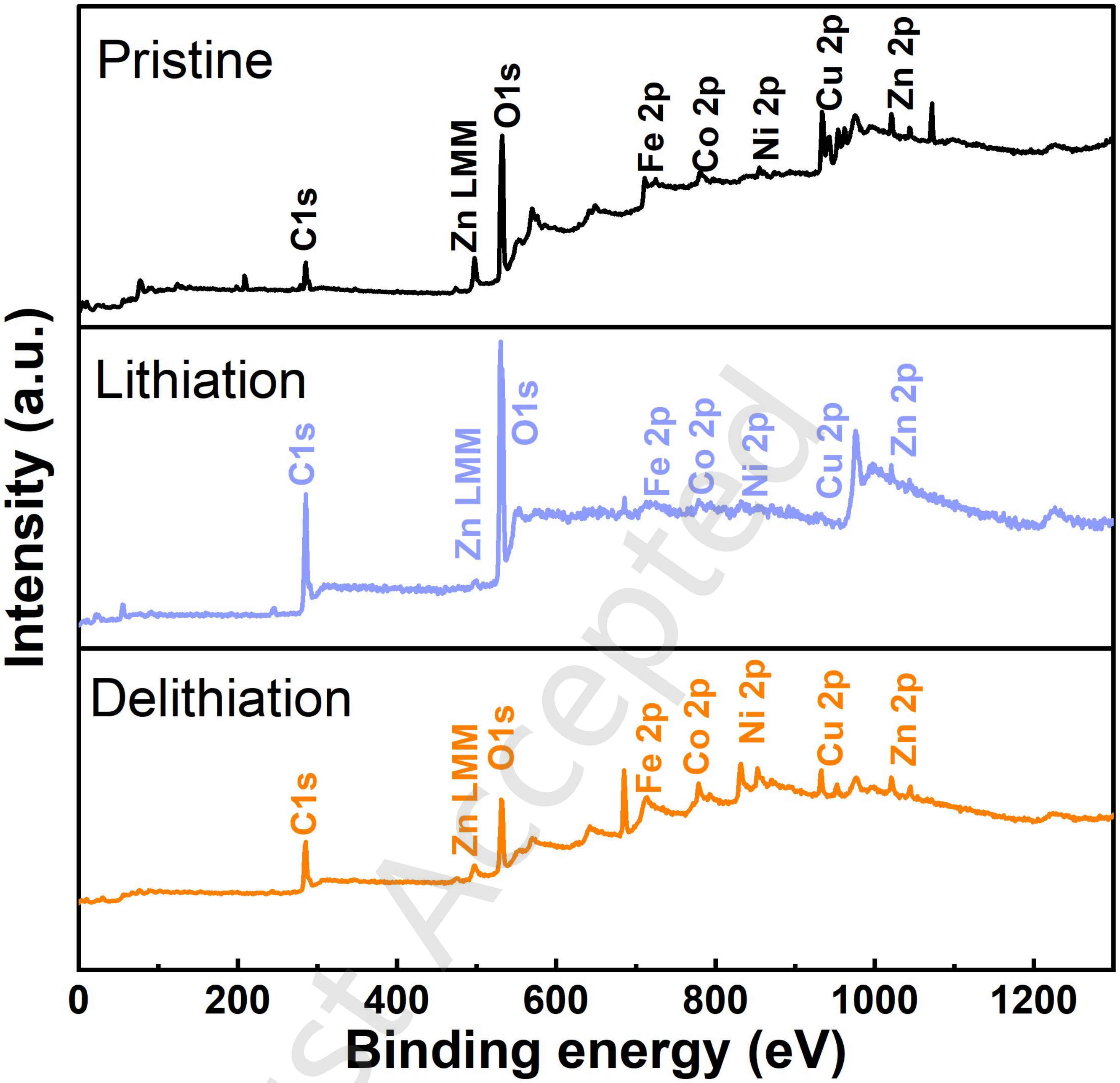

Figure S11 HEO XPS full spectra in different states.

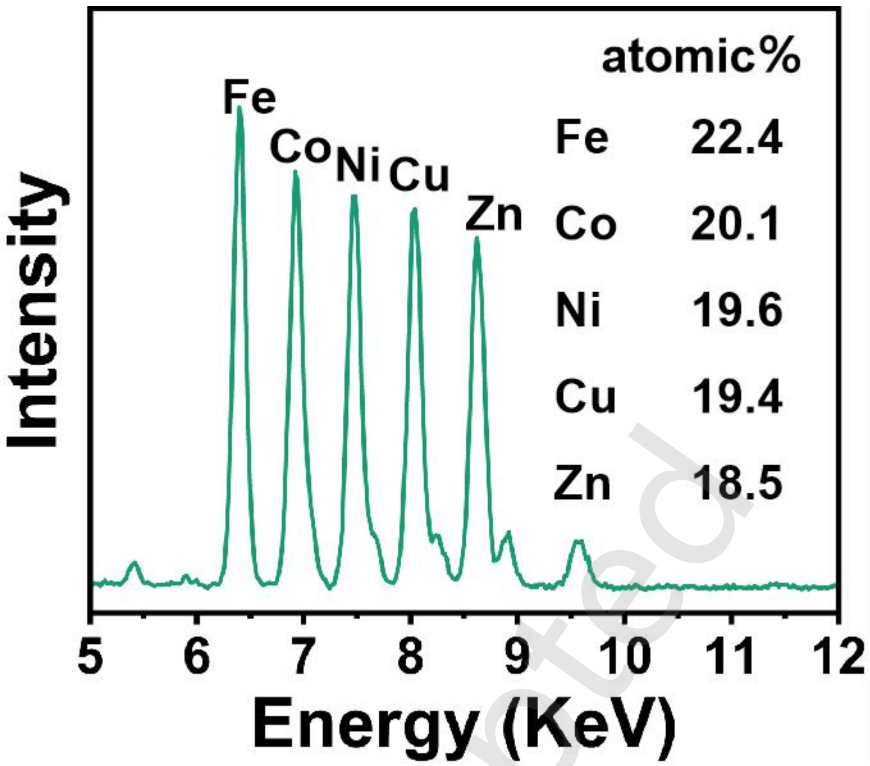

Figure S12 The intensity line plot and elemental scale analysis in STEM-EDS of HEO after 1000 cycles.

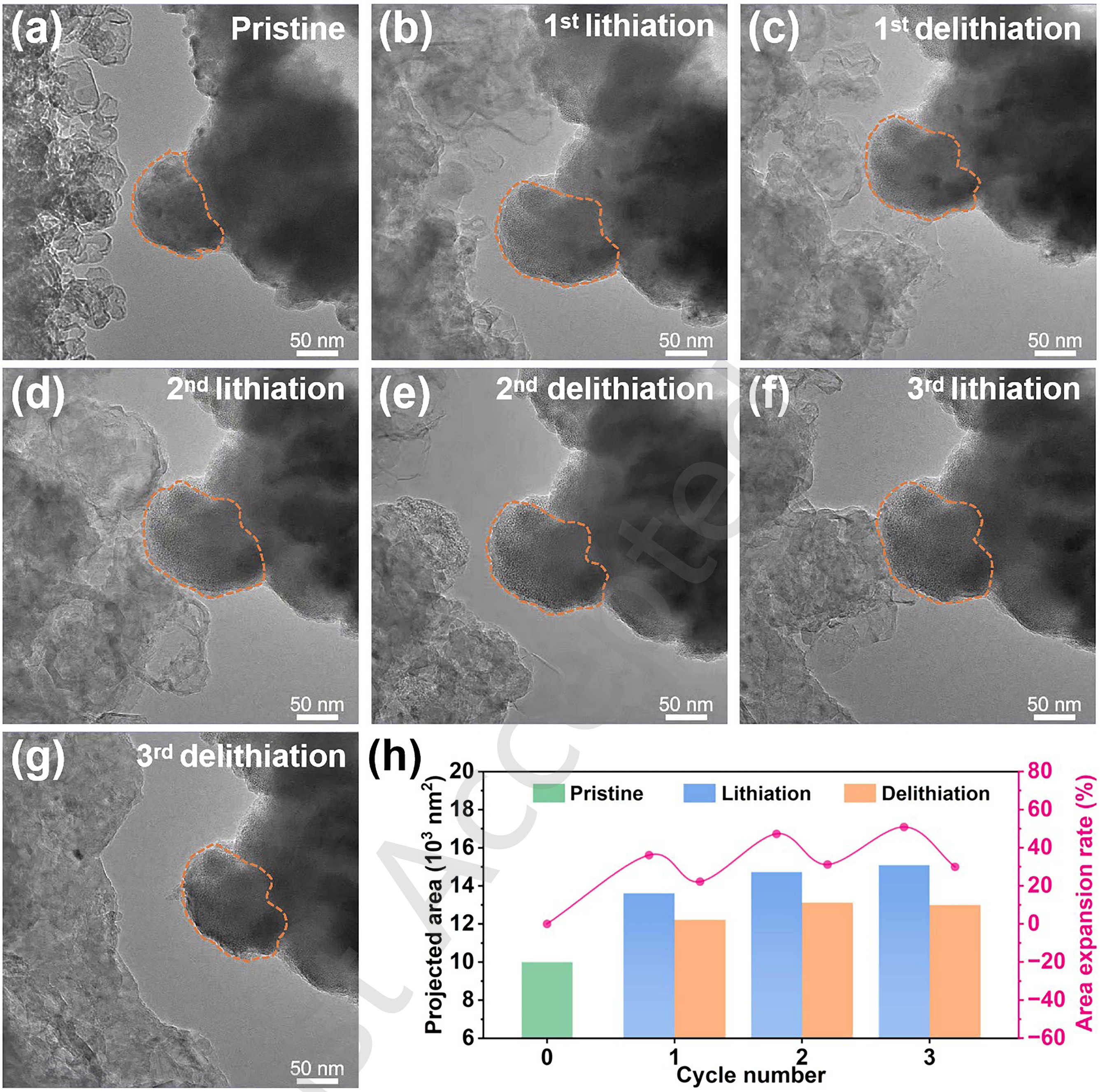

Figure S13 *In-situ* TEM observation of the initial three lithiation and delithiation cycles of the HEO. (a-g) Morphological changes of a single NP during its initial three lithiation and delithiation cycles. (h) In *in-situ* TEM images, the changes in projected area and area expansion rate of HEO particles during (de)lithiation.

3. Supplementary Tables

Table S1 Results of ICP-OES measured elemental ratios in HEO.

Element	Co	Fe	Ni	Cu	Zn
Relative atomic mass (g/mol)	58.933	55.845	58.693	63.546	65.38
Ppm (mg/L)	3.149	2.468	3.058	3.105	4.145
Atomic (%)	20.40	16.87	19.89	18.65	24.19

Table S2 Compare the electrochemical performance of previously reported HEO anodes with this work.

Composition	**Specific capacity (mAh/g)**	**Cycle number**	**Current density (mA/g)**	**References**
(FeCoNiCuZn)O	**947**	**1000**	**3000**	**This work**
$(FeNiCrMnCu)_3O_4$	**480**	**400**	**2000**	**1**
$(FeNiCrMnZn)_3O_4$	**680**	**200**	**500**	**2**
(MgCoNiCuZn)O	**390**	**300**	**500**	**3**
$(CoMnVFeZn)_3O_4$	**500**	**2000**	**3000**	**4**
(CoFeNiMnZn)O	**770**	**200**	**100**	**5**
$(FeNiCrMnCu)_3O_4$	**660**	**150**	**500**	**6**
(CoCuMgNiZn)O	**600**	**300**	**200**	**7**
$(FeNiCrMnCo)_3O_4$	**597**	**1200**	**2000**	**8**
$(FeNiCrMnCo)_3O_4$	**500**	**40**	**2000**	**9**
$(FeNiCrMnCo)_3O_4$	**751**	**200**	**500**	**10**
$(FeNiMnCuCoZn)_3O_4$	**628**	**100**	**200**	**11**
$(FeNiCuCoMg)_3O_4$	**907**	**300**	**2000**	**12**
$(LiFeNiMnCoZn)_3O_4$	**725**	**35**	**3000**	**13**
(MgCoNiCuZn)O	**417**	**300**	**1000**	**14**
(MgCoNiCuZn)O	**296**	**25**	**2000**	**15**

Supporting References

[1] Patra, J.; Nguyen, T.X.; Tsai, C.C.; Clemens, O.; Li, J.; Pal, P.; Chan, W.K.; Lee, C.H.; Chen, H.Y.T.; Ting, J.M., et al. Effects of elemental modulation on phase purity and electrochemical properties of Co‐free high‐entropy spinel oxide anodes for lithium‐ion batteries. *Adv. Funct. Mater*. **2022**, *32*, 2110992.

[2] Nguyen, T.X.; Patra, J.; Tsai, C.C.; Xuan, W.Y.; Chen, H.Y.T.; Dyer, M.S.; Clemens, O.; Li, J.; Majumder, S.B.; Chang, J.K., et al. Secondary‐phase‐induced charge–discharge performance enhancement of Co‐free high entropy spinel oxide electrodes for Li‐ion batteries. *Adv. Funct. Mater*. **2023**, *33*, 2300509.

[3] Triolo, C.; Xu, W.; Petrovičovà, B.; Pinna, N.; Santangelo, S. Evaluation of entropy‐stabilized ($Mg_{0.2}Co_{0.2}Ni_{0.2}Cu_{0.2}Zn_{0.2}$)O oxides produced via solvothermal method or electrospinning as anodes in lithium‐ion batteries. *Adv. Funct. Mater*. **2022**, *32*, 2202892.

[4] Hou, S.; Su, L.; Wang, S.; Cui, Y.; Cao, J.; Min, H.; Bao, J.; Shen, Y.; Zhang, Q.; Sun, Z., et al. Unlocking the origins of highly reversible lithium storage and stable cycling in a spinel high‐entropy oxide anode for lithium‐ion batteries. *Adv. Funct. Mater*. **2023**, *34*, 2307923.

[5] Su, L.; Ren, J.; Lu, T.; Chen, K.; Ouyang, J.; Zhang, Y.; Zhu, X.; Wang, L.; Min, H.; Luo, W., et al. Deciphering structural origins of highly reversible lithium storage in high entropy oxides with in situ transmission electron microscopy. *Adv. Mater*. **2023**, *35*, 2205751.

[6] Luo, X.F.; Patra, J.; Chuang, W.T.; Nguyen, T.X.; Ting, J.M.; Li, J.; Pao, C.W.; Chang, J.K. Charge-discharge mechanism of high-entropy Co-free spinel oxide toward Li^+ storage examined using operando quick-scanning X-ray absorption spectroscopy. *Adv. Sci*. **2022**, *9*, 2201219.

[7] Sarkar, A.; Velasco, L.; Wang, D.; Wang, Q.; Talasila, G.; De Biasi, L.; Kubel, C.; Brezesinski, T.; Bhattacharya, S.S.; Hahn, H., et al. High entropy oxides for reversible energy storage. *Nat. Commun*. **2018**, *9*, 3400.

[8] Xiao, B.; Wu, G.; Wang, T.; Wei, Z.; Sui, Y.; Shen, B.; Qi, J.; Wei, F.; Zheng, J. High-entropy oxides as advanced anode materials for long-life lithium-ion batteries. *Nano Energy*. **2022**, *95*, 106962.

[9] Nguyen, T.X.; Patra, J.; Chang, J.-K.; Ting, J.-M. High entropy spinel oxide nanoparticles for superior lithiation–delithiation performance. *J. Mater. Chem. A*. **2020**, *8*, 18963-18973.

[10] Huang, C.-Y.; Huang, C.-W.; Wu, M.-C.; Patra, J.; Xuyen Nguyen, T.; Chang, M.-T.; Clemens, O.; Ting, J.-M.; Li, J.; Chang, J.-K., et al. Atomic-scale investigation of lithiation/delithiation mechanism in high-entropy spinel oxide with superior electrochemical performance. *Chem. Eng. J*. **2021**, *420*, 129838.

[11] Dong, Q.; Hong, M.; Gao, J.; Li, T.; Cui, M.; Li, S.; Qiao, H.; Brozena, A.H.; Yao, Y.; Wang, X., et al. Rapid synthesis of high-entropy oxide microparticles. *Small*. **2022**, *18*, 2104761.

[12] Wang, X.L.; Kim, E.M.; Senthamaraikannan, T.G.; Lim, D.-H.; Jeong, S.M. Porous hollow high entropy metal oxides ($NiCoCuFeMg)_3O_4$ nanofiber anode for high-performance lithium-ion batteries. *Chem. Eng. J*. **2024**, *484*, 149509.

[13] Liu, X.; Yu, Y.; Li, K.; Li, Y.; Li, X.; Yuan, Z.; Li, H.; Zhang, H.; Gong, M.; Xia, W., et al. Intergrating hollow multishelled structure and high entropy engineering toward enhanced mechano-electrochemical properties in lithium battery. *Adv. Mater*. **2024**, *36*, 2312583.

[14] Liu, X.; Xing, Y.; Xu, K.; Zhang, H.; Gong, M.; Jia, Q.; Zhang, S.; Lei, W. Kinetically accelerated lithium storage in high-entropy (LiMgCoNiCuZn)O enabled by oxygen vacancies. *Small*. **2022**, *18*, 2200524.

[15] Wang, W.; Song, W.; Li, Y.; Guo, Y.; Yang, K.; Yu, L.; Xie, F.; Ren, Q.; He, K.; Wang, S., et al. Mesocrystallinely stabilized lithium storage in high-entropy oxides. *Nano Energy*. **2024**, *124*, 109482.